

Report D15.5 Report on diagnostic analysis and condition assessment

PROMOTiON – Progress on Meshed HVDC Offshore Transmission Networks
Mail info@promotion-offshore.net
Web www.promotion-offshore.net

This result is part of a project that has received funding from the European Union's Horizon 2020 research and innovation programme under grant agreement No 691714.

Publicity reflects the author's view and the EU is not liable of any use made of the information in this report.

CONTACT

Cornelis Plet – DNV GL
cornelis.plet@dnvgl.com
Uwe Riechert – ABB Switzerland Ltd
uwe.rieichert@ch.abb.com

DOCUMENT INFO SHEET

Document Name: Report on diagnostic analysis and condition assessment
Responsible partner: TU Delft
Work Package: WP 15
Work Package leader: Uwe Riechert
Task: 15.5
Task lead: Armando Rodrigo Mor – TU Delft

DISTRIBUTION LIST

APPROVALS

	Name	Company
Validated by:		
Task leader:	Armando Rodrigo Mor	TU Delft
WP Leader:	Uwe Riechert	ABB Switzerland Ltd

DOCUMENT HISTORY

Version	Date	Main modification	Author
1.0	24-02-2020	TU Delft	Armando Rodrigo Mor
2.0	24-07-2020	TU Delft	Armando Rodrigo Mor

WP Number	WP Title	Person months	Start month	End month
15	HVDC GIS Technology Demonstrator	164.5	23	48

Deliverable Number	Deliverable Title	Type	Dissemination level	Due Date
15.5	Report on diagnostic analysis and condition assessment	Report	Public	M48

LIST OF CONTRIBUTORS

Work Package and deliverables involve a large number of partners and contributors. The names of the partners, who contributed to the present deliverable, are presented in the following table.

PARTNER	NAME
TU Delft	Armando Rodrigo Mor, Luis Carlos Castro Heredia, Fabio Andrés Muñoz
ABB	Uwe Richert, Michael Gatzsche
DNV GL	Hong He, Nadew Belda.
SIG	Thanh Vu, Caterina Toigo
TenneT	Maximilian Tuzcek

CONTENT

- Document info sheet i
 - Distribution list i
 - Approvals i
 - Document history i
- List of Contributors ii
- Nomenclature 3
- Executive Summary 4
- 1 Introduction - PD Monitoring on GIS 5
- 2 partial discharge detection method on HVGIS based on magnetic field antennas 6
 - 2.1 The magnetic antenna 6
 - 2.1.1 Fundamentals 6
 - 2.1.2 Numerical simulations 7
 - 2.2 Magnetic antenna characterization 9
 - 2.3 Laboratory Experiments 12
 - 2.3.1 Test setup 12
 - 2.3.2 Detection 13
 - 2.3.3 Sensitivity 14
- 3 Charge estimation 1
- 4 Localization 4
- 5 Post-processing technique for noise discrimination 6
 - 5.1 Noise rejection techniques 7
 - 5.2 PD pulses and noise signals 7
 - 5.3 The cross wavelet transform 8
 - 5.4 Experimental setup 10
 - 5.5 Features extraction 12
 - 5.6 SVM classifier 14
- 6 Testing of the PD monitoring system in An ABB 320 kV HVDC GIS 16
 - 6.1 Results 18
 - 6.2 Sensitivity 20
 - 6.3 Charge estimation 21
 - 6.4 Localization 23

7 Conclusion.....25

8 Bibliography.....26

NOMENCLATURE

ABBREVIATION	EXPLANATION
D15.5	PROMOTioN deliverable 15.5
GIS	Gas Insulated System / Switchgear
HF	High frequency range
HFCT	High Frequency Current Transformer
HVAC	High Voltage Alternating Current
HVDC	High Voltage Direct Current
PD	Partial Discharge
PRPD	Phase-resolved PD Pattern
RF	Radio Frequency
UHF	Ultra High Frequency
VHF	Very High Frequency
WP	Working package

EXECUTIVE SUMMARY

Offshore wind energy plays a crucial role in the energy transition, in which the North Sea is an excellent place to install wind turbines due to its relatively shallow waters, its favourable wind climate, and its proximity to energy consumers [1]. This need for offshore wind energy yields a higher demand for DC GIS technology, and in turn, this implies increasing demands on components, materials, and monitoring and diagnostics (M&D) tools.

The EU funded project "Progress on Meshed HVDC Offshore Transmission Networks" (PROMOTioN) addresses the challenges for meshed HVDC offshore network development, aiming for an increase in the Technology Readiness Level (TRL) for HVDC GIS. Few HVDC GIS are in operation worldwide, resulting in little service experience and information about the long-term capability of this technology. The Working Package 15 (WP15) performed a DC GIS Technology Demonstrator to tackle this lack of laboratory and field experience as a way to anticipate oncoming needs. Several cornerstone tasks have been defined to achieve such a goal, which include research on monitoring and diagnostics techniques for HVDC GIS (deliverable D15.3 and D15.5).

Gas Insulated Systems (GIS) have shown high reliability and low failure rates, becoming the most suitable technology for the future DC systems. However, failures in offshore installations are more critical and expensive than in their onshore counterparts. For this reason, the measurements of partial discharges (PD) are used worldwide by GIS manufacturers and utilities for the detection of incipient defects as an important part of the monitoring and diagnostics (M&D) of HV GIS. Not only for M&D purposes but also to understand the dielectric properties of alternative gases that will soon replace SF₆.

Conventionally PD measurements on GIS have relied on several broadband techniques to detect the electromagnetic waves produced by a PD event. Standards as the IEC62478 advise on the set-ups and working frequency ranges (VHF/UHF), while other documents such as the CIGRE WG. D1.25 defines a "sensitivity check" procedure to verify that a VHF/UHF measuring system on-field can pick up signals equivalent to 5 pC as measured by the conventional IEC 60270 method during laboratory tests. To present, the VHF/UHF methods are the standard for AC GIS and are expected to migrate to offshore DC GIS installations. They, indeed, have gained popularity because of their high local sensitivity and noise rejection. However, the PD signals in the UHF range are heavily attenuated with distance, pressing to install UHF coupler every few meters. The intrinsic nature of the detection and the attenuation also make it impossible to quantify PD parameters, such as the apparent charge.

TU Delft in WP15 has been researching complementary PD detection techniques that can mitigate the limitations of the reduced spatial sensitivity and PD parameter quantification of the traditional UHF methods. Such alternative and complementary technique concerns the broadband magnetic detection of PD conduction currents. In D15.3, experimental results demonstrated the feasibility of picking up by magnetic means the conduction currents flowing along the GIS compartment upon a PD event. Those results steered our research towards the design of a magnetic antenna for PD detection. In this report D15.5, We describe details of the antenna design, signal conditioning circuitry, signal acquisition, and the post-processing techniques needed for PD detection, quantification and localization.

The Cross Wavelet Transform (XWT) and Support Vector Machines (SVM) were used to separate PD signals from noise and external disturbances, which are more likely to affect the signal acquisition due to the broad bandwidth of the magnetic detection. A calibration factor relating the charge of a PD source and the response of magnetic sensors in the GIS compartments has been determined experimentally in an AC and DC GIS, marking a milestone in the state-of-the-art. In addition, it has been proven how this magnetic approach boosts the spatial sensitivity by seizing the lower attenuation with distance in the low-frequency range of the PD signals. Such findings entail that few sensors will be eventually needed to cover the full GIS. It is also advantageous that the magnetic antennas are simply two hemi-circle loops in a mirror-like disposition that can be placed in the UHF coupler windows already existing in the compartments of both AC and DC GIS.

The experimental results reported in this document, as well as in the several journal papers published in the development of PROMOTioN project, were obtained from two actual-size GIS, one at the High Voltage Lab of TU Delft and the other from an ABB HVDC GIS at Kema Labs.

1 INTRODUCTION - PD MONITORING ON GIS

Partial discharge measurements can be carried out in HVDC GIS following the traditional UHF method, as described in [2]. However, the UHF method is not able to accurately estimate the apparent charge due to the frequency bandwidth of the sensors and the propagation modes in the UHF range in the GIS. Moreover, at high frequency, the attenuation of the signals in the UHF is prominent, which means that the distance between the UHF antennas has to be carefully considered to ensure a good sensitivity in the whole GIS. The signal attenuation is due to the GIS components, like spacers [3], disconnecting elements [4], T-branches[5], L-branches [6] and in general due to any installed element that either creates a geometrical or material change.

To overcome these limitations, a new method based on magnetic antennas has been developed at Delft University of Technology. The foundations of the method have been presented in [7]. The magnetic antennas consist of two shielded loops that can be installed in the existing coupler windows where the UHF antennas are connected. When a partial discharge propagates through the GIS, the induced currents in the GIS compartment have to diverge as they encounter the opening of the coupler window. The charge in the direction of the currents surrounding the coupler window induces a magnetic field that is picked up by two shielded coils. The shielded coils are arranged in such a way that one coil measures the flux created in the upper part of the opening, and the other coil measures the flux in the lower part, both with respect to the propagation direction of the partial discharge. Since the induced partial discharge currents flowing in the GIS are homogeneously distributed, both antennas measure opposite polarity signals of similar magnitude. This fact helps in recognition of the partial discharges, since external coupled noise does typically not induce a symmetric voltage in the antennas.

Due to their constructive aspects, the magnetic loop antennas work in the HF and low VHF range [8]. In practice, due to the geometry and dimensions of typical HVDC GIS, this means that the antennas measure the portion of the partial discharge signal that propagates in the transverse electromagnetic mode (TEM). In this frequency range, the signal attenuation is smaller than in the UHF range. In laboratory experiments, the sensitivity of the magnetic loop antennas is in the order of magnitude of 5 pC at 3.3 m distance for a free moving particle in SF₆.

Since the measuring system uses the HF and VHF range, a normal partial discharge calibrator can be used to perform the sensitivity check and the charge calibration. Since the antennas are based on magnetic detection, it is advisable not to mount the antennas close to GIS ends or terminations. Otherwise, the reflected currents due to the impedance mismatching will reduce the sensitivity of the antenna. In that regard, a minimum distance around 1.5 m to the GIS terminations or ends is recommended for the magnetic antenna location.

The charge calibration of the magnetic antenna can be done by using a mathematical method that performs the double-time integral of the measured signals affected by a calibration factor. This calibration factor can be experimentally determined using a calibration rig. At Delft University of Technology, a testbench has been built to perform the calibration. The testbench is a calibration rig that uses a small GIS compartment reproduction in which the inner conductor has been adapted to mount a high frequency current transformer [8]. Using the high frequency current transformer and applying the double-time integral of the measured signal, the calibration constant is experimentally determined. The calibration should inject a PD pulse with a broader frequency content than the magnetic loop antenna, which in practice means that a partial discharge calibrator for cable testing is suitable. The calibration factor heavily depends upon the GIS dimensions; therefore, it can only be used in partial discharge GIS measurements that use GIS tubes or the same dimensions. The experimentally determined calibration constant has been checked in laboratory experiments using real GIS and test cells equipped with current measurements for charge reference[8]. The experiments show small deviations between the antennas and between them and the test cell reference up to 30% maximum differences. This deviation is attributed to small differences in the orientation and position of the antennas in the real GIS coupler window to the calibration rig.

2 PARTIAL DISCHARGE DETECTION METHOD ON HVGIS BASED ON MAGNETIC FIELD ANTENNAS

In this report, a new concept of PD detection on GIS based on a novel magnetic antenna that measures the magnetic field produced by partial discharges (PD) propagating along the GIS compartments is proposed. The fundamentals of the detection technique and the magnetic antenna design are presented together with laboratory measurements in the following sections. The performance and the sensitivity of the detection with the magnetic antennas proved its suitability for PD detection and apparent charge estimation.

2.1 THE MAGNETIC ANTENNA

2.1.1 FUNDAMENTALS

A partial discharge produces electromagnetic radiation in a broad bandwidth ranging from DC to GHz. Inside a GIS compartment, the electromagnetic radiation induces currents in the main conductor and in the external enclosure. The PD current flows along the GIS as a surface current due to the electromagnetic wave high frequency content. This current travels through the electrical paths in the GIS, such as the spacers, the L branches, T joints, circuits breakers, or any other path in the GIS. When the GIS uses external-type spacers as it is the case of the one at TU Delft, the compartments are electrically connected to each other by bridges, as well as, by bolts to allow the pulse propagation. During the propagation, the current suffers attenuation, reflections, and dispersion.

In the GIS enclosure, the surface current distribution is homogeneous due to its coaxial structure, as is presented in Figure 1. The coaxial structure also entails that the PD signals will travel along the GIS regardless the connections to ground due to the higher impedance of the ground paths (see D15.3). When the surface current reaches the coupler window, the PD current loses its homogeneity and travels around the window. This deviation around the coupler window produces a magnetic field normal to the window surface. The PD current has a transient behavior; then, the coupler window magnetic field is time-variant. Figure 2 shows that this magnetic field induces an electric field in the coupler window surface. Therefore, if a conductive closed loop is placed in the coupler window, it will eventually have an induced voltage caused by the PD pulse traveling in the GIS compartments, as is presented in Figure 3. It is worth

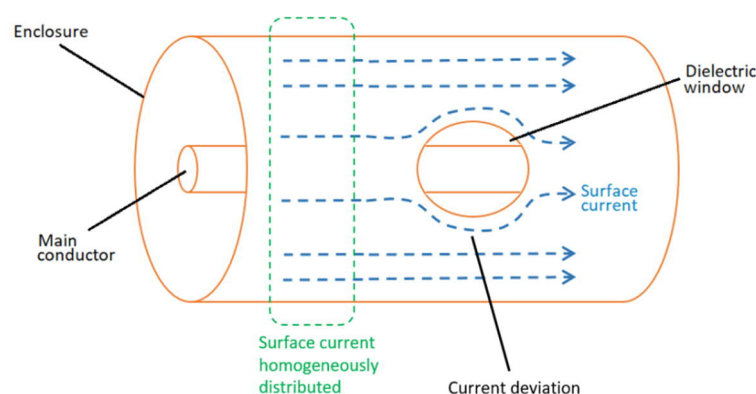


Figure 1. Surface current distribution in the GIS enclosure.

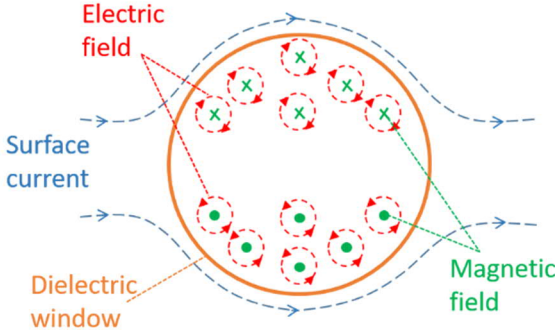


Figure 2. Magnetic field and induced electric field in the coupler window.

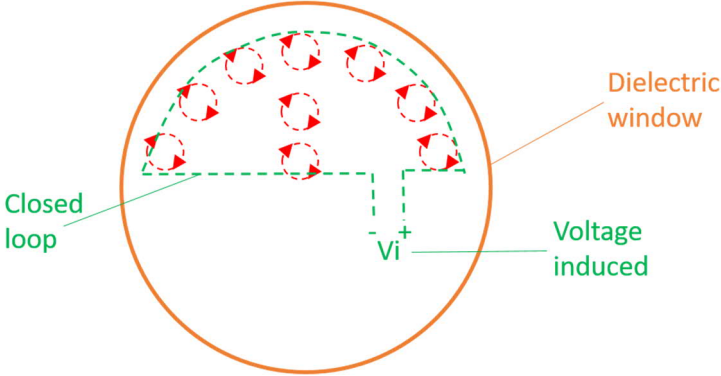


Figure 3. Voltage induced in a closed loop.

2.1.2 NUMERICAL SIMULATIONS

The hypothesis presented in the section above was initially tested using the Finite Element Method (FEM) in a GIS compartment having only the main conductor, the external enclosure, and a coupler window. For the FEM model, a 3D geometry, a radio-frequency physics, and a time dependent study were chosen. The PD pulse was injected through a lumped port set as a coaxial cable in one of the compartments ends, while the remaining end was given a lumped port in off condition. The geometry, the lumped ports, and the PD pulse are presented in Figure 4. The model dimensions are given in Table 1. The time-dependent simulation was set in a time range adjusted between 0 ns and 5 ns in 0.01 ns steps.

Table 1. Model dimensions.

Component	Radius	Length
Enclosure	560 mm	500 mm
Main conductor	140 mm	500 mm
Coupler window	110 mm	---

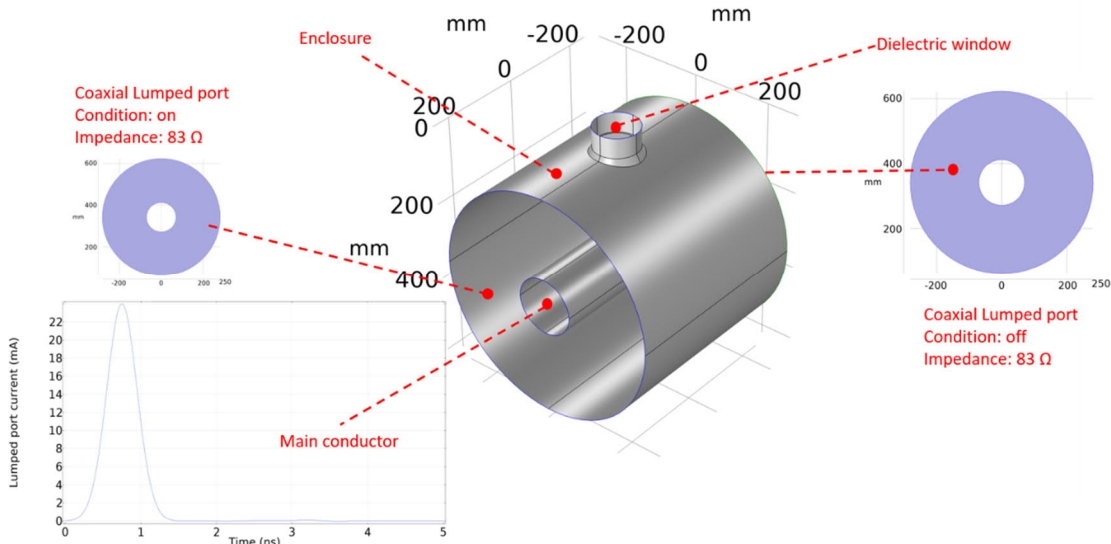


Figure 4. Geometry and ports configurations.

Figure 5 shows the evolution of the surface current in the enclosure. Before the PD pulse reaches the window, at 1 ns, the surface current distribution is homogeneous. Then, at 1.5 ns, the current arrives at the window and suffers a deviation around it. This current deviation causes a perpendicular magnetic field in the coupler window, which is shown in Figure 6.

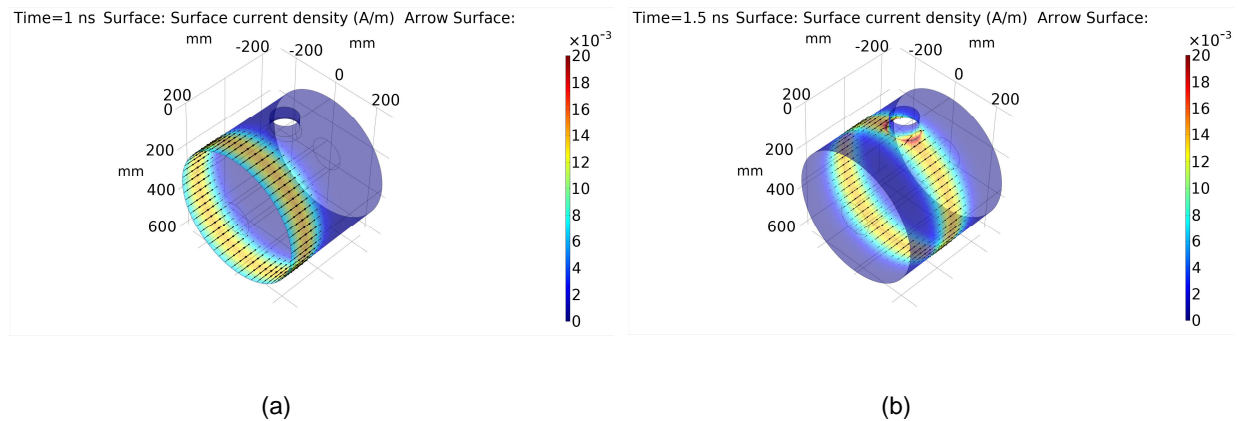


Figure 5. Surface current temporal evolution at 1 ns and at 1.5 ns.

According to the results in Figure 6, the magnetic field distribution presents an odd-symmetry, meaning that half-window has the same magnetic field that the other one but with the opposite direction. This fact indicates that there is a net magnetic flux "piercing" only half-window because the net flux through the whole window is zero. Therefore, it is possible to obtain an induced voltage using a conductive loop placed in only half-window. Figure 7 presents the voltage generated for the PD pulse in half-window, having an amplitude in the tens of mV.

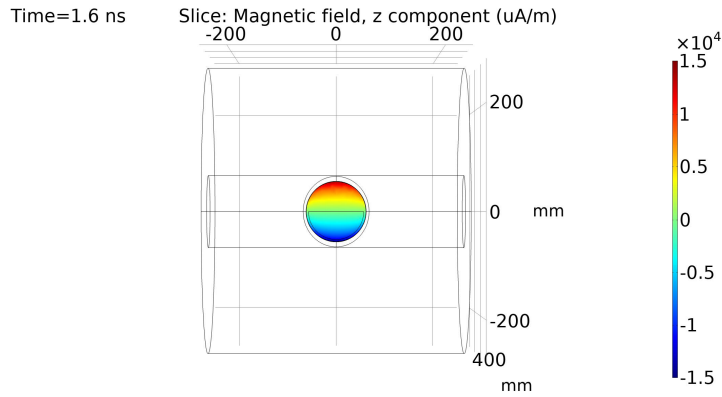


Figure 6. Magnetic flux density perpendicular to the coupler window at 1.6 ns.

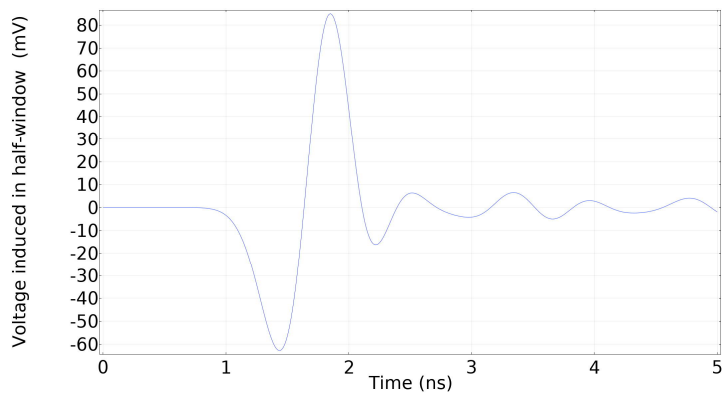


Figure 7. Voltage induced in half-window.

In conclusion, the numerical results indicate that the PD pulses generate a surface current, which can be measured in the coupler window, where the traditional VHF/UHF antennas for partial discharges detection are located. Based on these results, a new PD measuring system has been developed based on a magnetic loop antenna placed in half-window. The following section will focus on the magnetic antenna technical aspects and in the characterization of the aforementioned magnetic sensor.

2.2 MAGNETIC ANTENNA CHARACTERIZATION

The magnetic antenna is made up of two shielded loops, as is presented in Figure 8. The loops were built in a half-circle shape using the coaxial cable RG179, which results in 218 nH inductance and 32 pF capacitance per loop. As is shown in Figure 8, a conductive mounting plate was added to the antenna to keep the internal Faraday cage capabilities of the GIS enclosure.



Figure 8. Magnetic antenna [9].

The magnetic antenna is meant to be placed in the existing coupler windows of the GIS enclosure, where the distance between the loops and the mounting plate is such that the antenna perimeter levels the edge of the internal wall of the coupler window with the internal GIS enclosure. A 2 mm clearance between the loops diameter and the inner walls of the coupler window has been chosen because the antenna installation must overcome the internal bump produced by the perimeter welding of the window pipe to the GIS compartment. The antenna diameter is 103 mm, and the distance to the mounting plate is 53 mm.

Ideally, the magnetic antenna loops (named as top and bottom loop) measures only the magnetic field produced by the PD current in the enclosure. However, it also measures the electric field produced by the PD pulse. The outer loop formed by the coaxial cable screen is only grounded in one side and left floating in the other to prevent short-loop currents and to provide electric field shielding. The inner loop formed by the inner coaxial cable conductor forms the measuring loop. It is connected to a parallel of $2 \times 0.056 \mu\text{F}$ decoupling capacitors and a commercial trans-impedance amplifier model Femto HCA-40M-100K-C. The decoupling capacitor was added to block the DC feedback loop between the amplifier and the magnetic antenna. The schematic circuit is presented in Figure 9, where L_{a1i} represents the inner conductor inductance, L_{a1o} the screen inductance, C_{ca1} is the loop capacitance due to the coaxial cable, C_{pa1} is the parasitic capacitance of floating end screen, L_{h1} is the inductance of the hole in the GIS coupler window, and $K1$, $K2$, and $K3$ are the coupling coefficients. L_{h1} and the coupling coefficients have been calculated using electromagnetic finite element simulations.

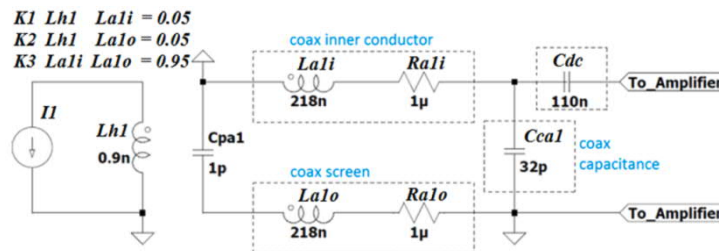


Figure 9. Magnetic antenna equivalent electric circuit [8].

A test bench, specially design for calibration purposes, was built to test the frequency response of the magnetic antenna and its associated components (decoupling capacitor + trans-impedance amplifier). Figure 10 presents the test bench, which was equipped with two cones for matching the impedance of the GIS enclosure, avoiding reflections, and allowing the injection of high-frequency currents. The test bench consists of three GIS compartments, a wire (1 mm diameter) as the main conductor, and the injection and termination cones. The input current flowing through the main conductor was measured using a HFCT, model FCT-016-5.0 from Bergoz with 3.92 kHz–1.11 GHz bandwidth.

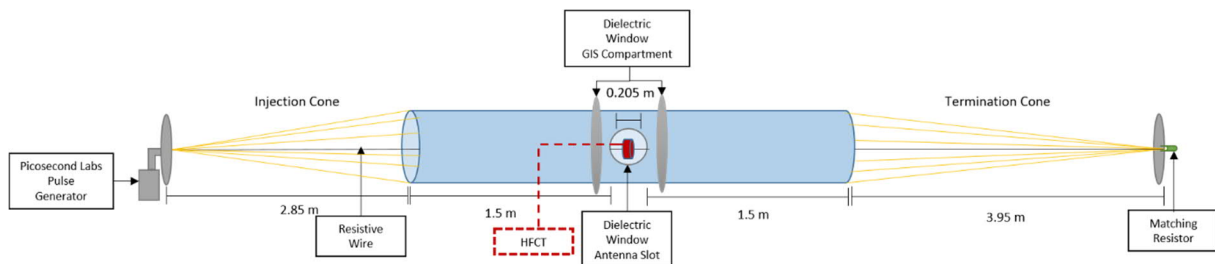


Figure 10. Test bench.

Figure 11 presents the input current in the time and frequency domain measured by the HFCT. The current pulse is a high-frequency and unipolar pulse injected with a pulse generator at the injection cone. The termination cone is not perfectly matched, causing small reflections of the current pulses, which interact with the unipolar-pulse jeopardizing the frequency response. For this reason, the main conductor was made with resistive wire that attenuates the reflections, causing a clear and unique current pulse.

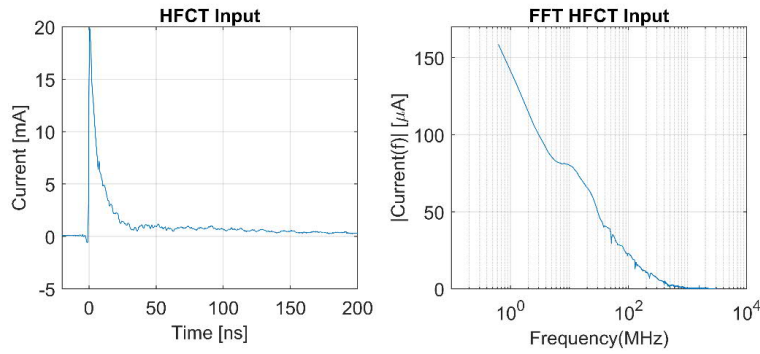


Figure 11. Input current pulse.

Figure 12 shows the output signal measured by one of the antenna loops. The frequency response of the magnetic antenna is presented in Figure 13.

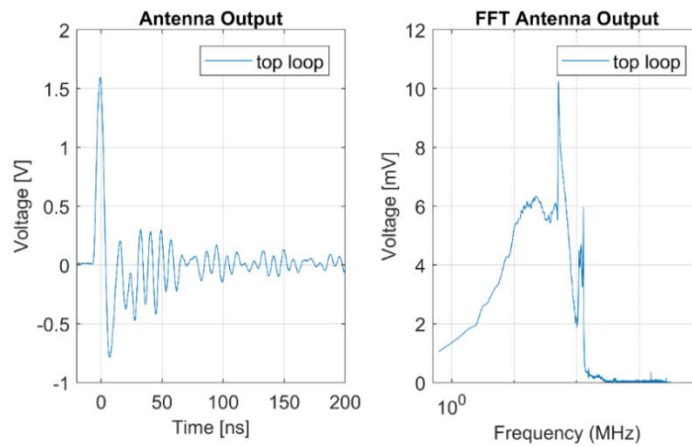


Figure 12. Magnetic antenna output signal.

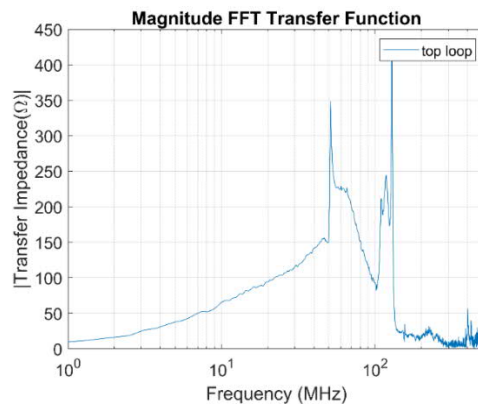


Figure 13. Magnetic antenna frequency response.

Some remarks about the magnetic antenna are given as follows:

- The frequency peaks are around 52 MHz and 125 MHz.
- The magnetic antenna is tuned at the High Frequency (HF) range, in opposition to the VHF and UHF ranges of the traditional electric antennas. This frequency range corresponds to the TEM propagation mode.

2.3 LABORATORY EXPERIMENTS

2.3.1 TEST SETUP

A set of three magnetic antennas were tested in a 380 kV AC GIS at the High Voltage Laboratory of TU Delft, where the SF₆ was removed from all the GIS compartments. The GIS in Figure 14 consists of multiple spacers, a T-joint branch, switchgear, a bushing, an L-branch connection, a disconnect switch, and eight coupler windows for PD monitoring equipped with UHF antennas. Three UHF were removed and replaced by magnetic antennas at the locations highlighted in Figure 14—two near the ends of the GIS and one in the middle point.

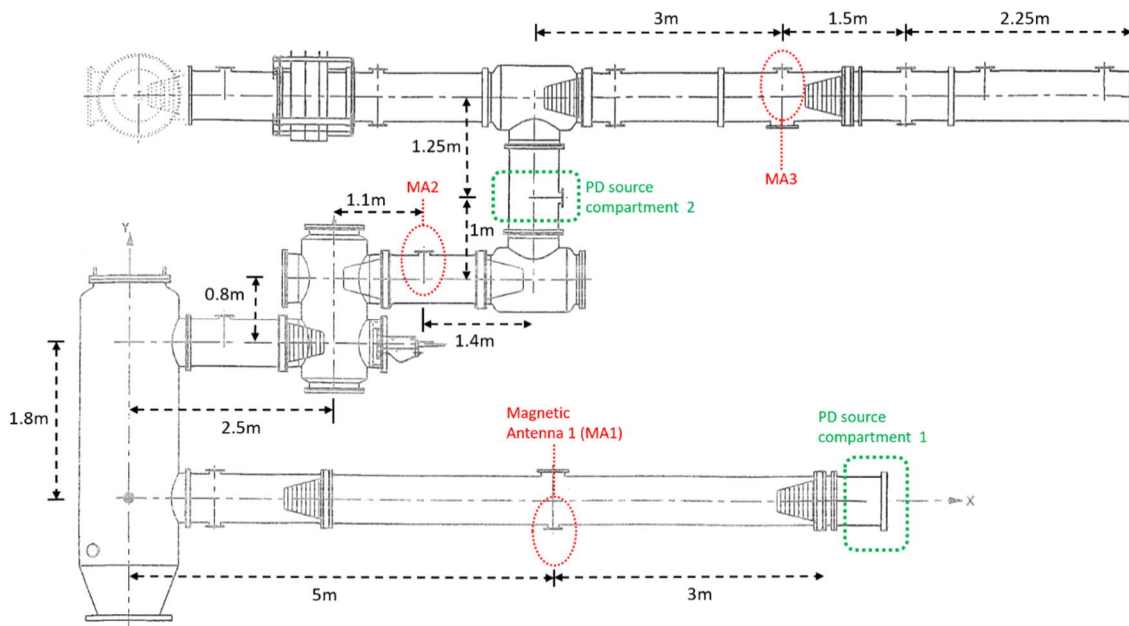


Figure 14. GIS map.

Inside the GIS, corona discharges were produced by two different sources, which were tested under DC negative voltage and separately (time-wise). The first corona source, named CS1, was built in a test cell under SF₆ at 100 kPa (relative). Figure 15 shows the test cell installed in the GIS compartment 1, where a HFCT (FCT-016-5.0 Bergoz) was installed in the rod holding the CS1 to record the PD current at the source. A 25.5 dB amplifier was connected to the HFCT output to improve the signal to noise ratio. The HFCT at the source permits the charge estimation at the source, which will be useful for the evaluation of the charge estimation in section 3.



Figure 15. Test cell at the GIS compartment 1[8].

The second corona source, CS2, consisted of a needle connected at the main conductor in compartment 2. This defect was only monitored by the magnetic antennas, meaning that the HFCT was not connected. The purpose of the test with CS2 was to evaluate the magnetic antenna capabilities for PD localization.

The PD signals were recorded using the Tektronix MSO58 oscilloscope in Fast Frame Acquisition Mode, which captures multiple PD pulses individually in a frame with a specific record length. The oscilloscope simultaneously sampled the HFCT and the magnetic antennas. Table 2 summarizes the different voltages and tests performed.

Table 2. Model dimensions.

Test	PD Source	Gas	Compartment having the PD source	DC Voltage
1	CS1	SF ₆ (100 kPA relative)	1	-10 kV
2	CS2	Air (atm)	2	-15 kV

2.3.2 DETECTION

This work uses a collection of 2 measurement results as described in 2.3.1, which are used to verify the magnetic antenna performance. In total, the oscilloscope acquired 7000 PD signals, where 5000 PDs corresponded to test 1, and 2000 to the test 2. The PD charge estimation was only possible in Test 1 because it had the HFCT directly connected to the test cell.

Figure 16 shows the apparent charge for the 5000 PD pulses collected in test 1 calculated from the HFCT. This setup resulted in PD charges ranging between 4 pC and 170 pC, which was helpful for the charge estimation analysis in section 3.

Figure 17 presents a characteristic PD pulse recorded by the magnetic antenna MA1 and the HFCT in test 1. The magnetic antenna signals show that the first peak of both loops appears around the same time (around 0.22 μ s), the signals have different polarities and a pseudo-mirror-like symmetry. An ideal mirror-like symmetry cannot be obtained due to the noise, the manufacturing differences between both loops and small misalignments of the antennas with respect to the coupler window.

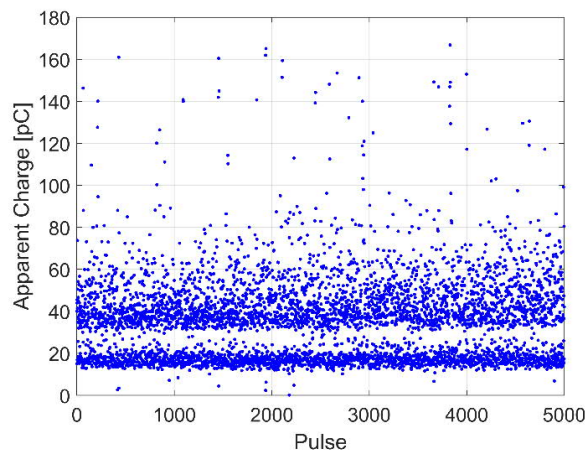


Figure 16. Apparent charge for each of the PD pulses recorded by the HFCT in test 1.

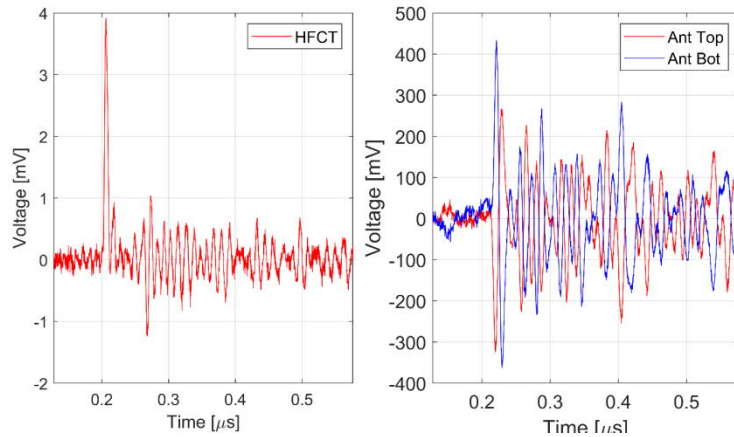


Figure 17. Example of a PD pulse measured by the HFCT and the magnetic antenna MA1.

2.3.3 SENSITIVITY

The magnetic antenna ability to detect PD pulses was tested using the results coming from test 1. This ability to detect PD pulses was proven by checking the minimum charge detection level of the closest magnetic antenna to the test cell and the farthest one. The checking of the minimum detection level was done following three criteria: the peak amplitudes of both loops were synchronized, its peak magnitude was roughly two times the background noise, and its average power indicates a clear pulse.

The closest magnetic antenna to the test cell, MA1, was able to detect PD pulses having charges above 5 pC. Figure 18 shows the PD pulse recorded by the HFCT and the corresponding signals recorded by the magnetic antenna loops at the closest location (MA1). From the signals, it can be confirmed that both peaks occurred at the same time, and the peak magnitudes are at least two times higher than the background noise. Regarding the average power, it shows two different zones: a flat zone at the beginning of the signal, followed by a significant rising of the power, where the flat zone corresponds to the background noise, and the increase of the power after the flat zone indicates the presence of the PD signal. On the other hand, the farthest antenna (MA3) could not detect this small PD, as is depicted in Figure 19. This is explained by the fact that the PD signals coming from the test cell split at the T branch, causing a reduction and distortion in the PD current flowing through the compartment where MA3 is installed, affecting the sensitivity of the antenna.

Nevertheless, the farthest antenna to the test cell was able to detect PD pulses having charges above 15 pC. Figure 20 shows the PD pulse recorded by the HFCT and the signal recorded by the magnetic antenna loops at MA3.

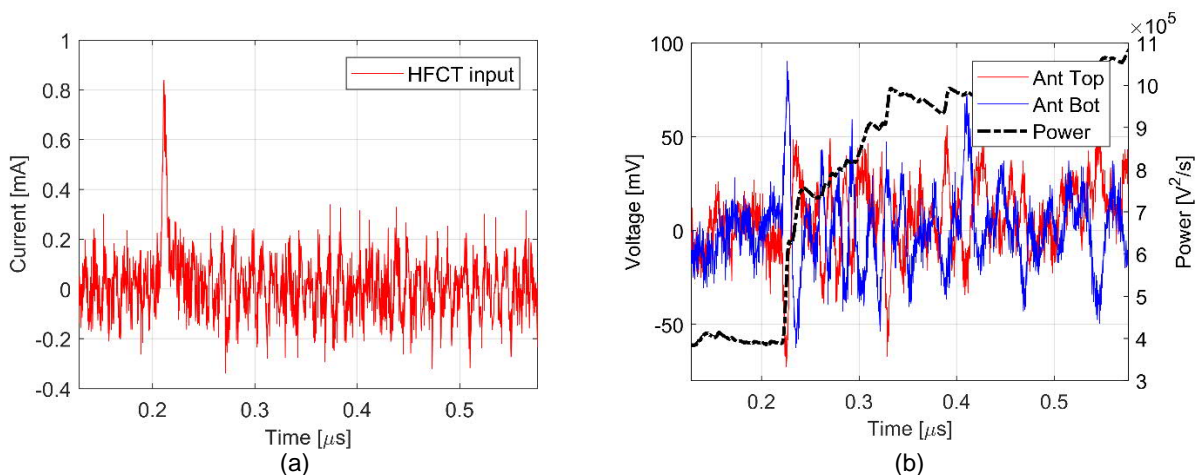


Figure 18. PD pulse measured by the HFCT of the smallest PD pulse (5 pC) detected at MA1.

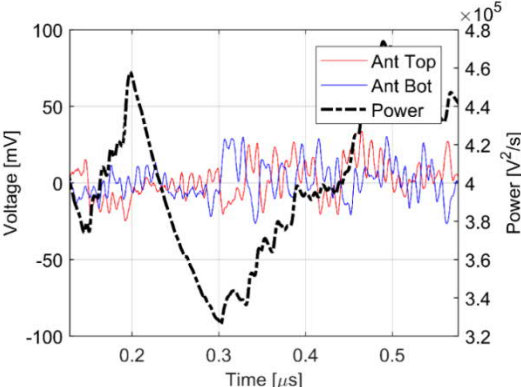
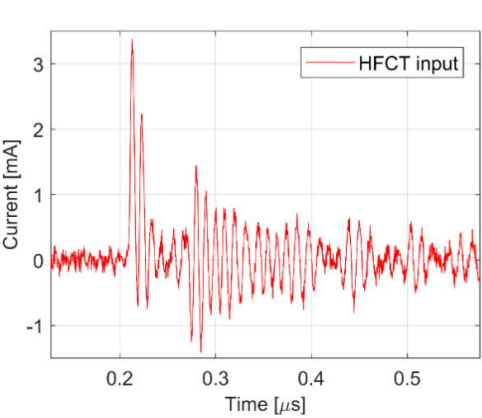
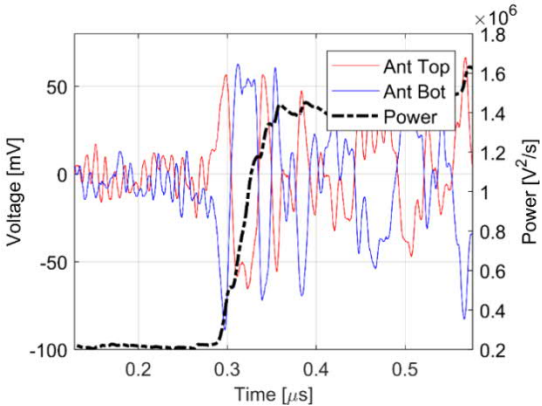


Figure 19. Smallest PD pulse (4.98 pC) measured by MA3.



(a)



(b)

Figure 20. PD pulse measured by the HFCT of the smallest PD pulse (15 pC) detected at MA3.

3 CHARGE ESTIMATION

This section aims to find the limits of charge estimation of the signals picked up by the antennas at position MA1, MA2 and MA3 in Figure 14 upon a PD event produced in the test cell in the compartment 1.

The charge estimation at different locations is studied as the comparison of the calculated value from the magnetic antenna and the reference charge value. For this purpose, the reference charge value is calculated as the discrete integral of the current output of the Bergoz HFCT connected next to the test cell. This arrangement of the HFCT ensures an acquisition with enough bandwidth and sufficient SNR (signal to noise ratio) such that the charge of the PD signal is estimated within an acceptable error.

Synchronous acquisition of all channels of the oscilloscope plays a vital role in a 1-to-1 comparison of the reference charge value and the antenna's charge value. Therefore, the HFCT signal is set to be the trigger of the oscilloscope, and the antenna's signals are acquired relative to a true PD signal in the test cell. This scheme reduces false triggers as well as results in signals with sufficient SNR. The dynamics of SF₆ lead to a broad range of PD amplitudes, which proves useful to test the error in the charge estimation.

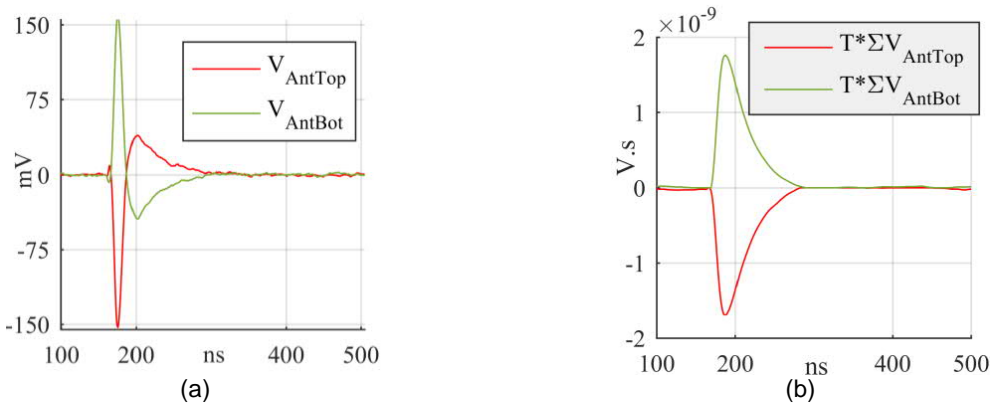


Figure 21. Determination of the pseudo-current of the antenna's output for charge estimation [8].

As reported in [8], the charge estimation from the antennas involves three steps. The first step is the discrete cumulative integration of the antenna's voltage output, as illustrated in Figure 21. This results in a pseudo-current signal that is then, in a second step, integrated to estimate the charge of such a pseudo-current. The third step consists of applying an experimental calibration factor [8] to calculate the charge equivalent to the total current flowing along the GIS compartment.

Important remarks are that the output of the antenna is a voltage signal, not a current signal; thus, its integration strictly does not yield a value of the charge. However, a charge value obtained after integrating the output voltage signal still holds because, as shown in Figure 22b, there is a linear dependency between the charge so obtained and the reference charge value.

The proportionality factor, or calibration factor K_c as it will be referred to in this document, was experimentally obtained using the calibration rig in Figure 22a. K_c is thus the ratio of the charge of known calibration pulses and the charge calculated from the antenna as per the aforementioned integration method.

The calibration factor was estimated as

$$K_c = 7.1862 \times 10^5 \left[\frac{C}{V \cdot s^2} \right]$$

In a second exercise, the antenna was installed in the GIS, and the calibration pulses were injected at a distance of 3.3 m. It was observed that compensation of $1.3 \cdot K_c$ adjusts better the reference charge and the charge estimated from the antenna's output.

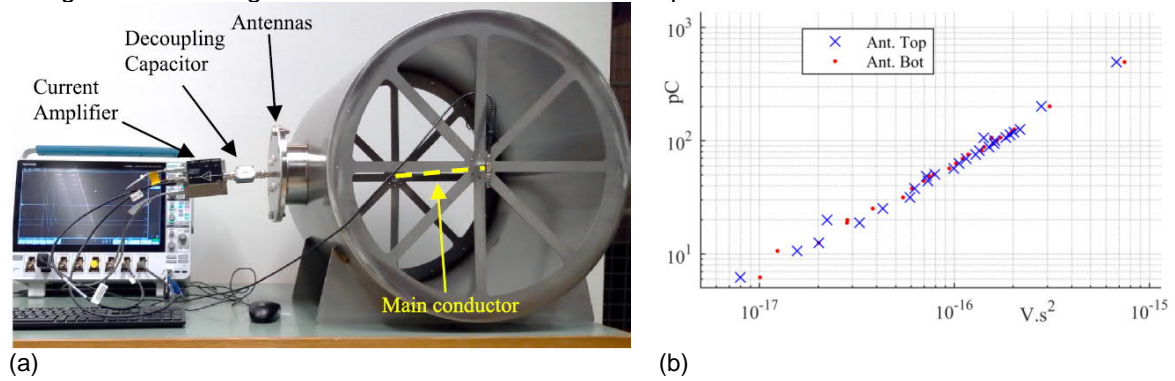


Figure 22. a) Calibration rig setup [8], b) Correlation between the reference charge and the charge as measured by the antennas.

The results of the charge estimation are shown in Figure 23 with the colormap indicating bins of error compared to the reference charge. For this analysis, only reference signals in the range from 10 to 30 pC were studied. This resulted in a subset of 1085 signals of out the total 5000 acquired signals. Limiting the data to this range of charge is preferred to test the sensitivity of the antennas.

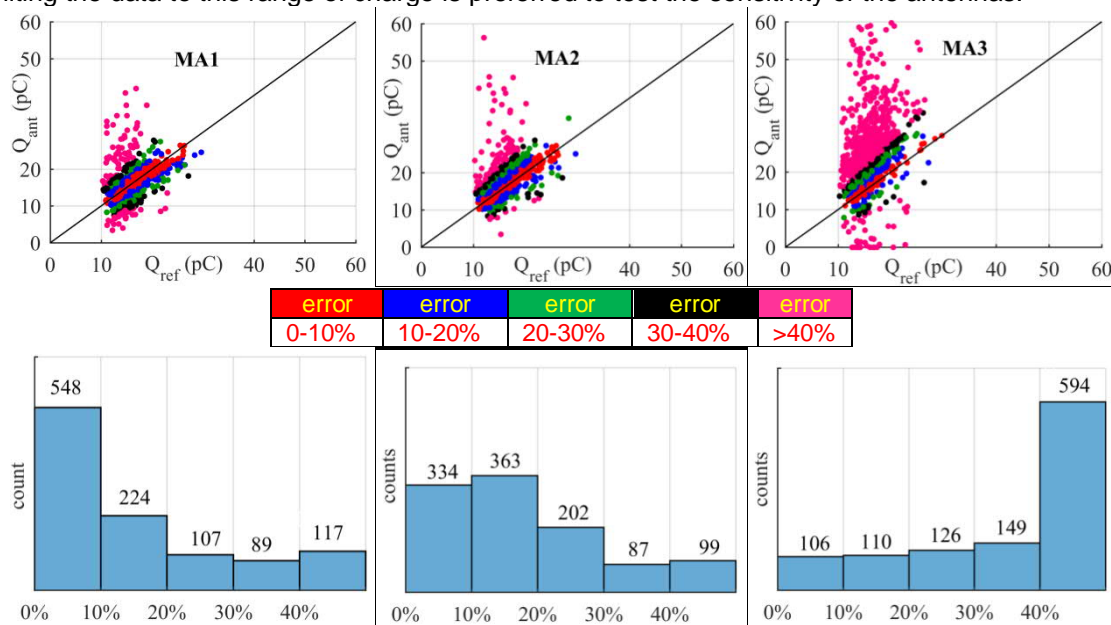


Figure 23. top) comparison of charge estimation at every location of the magnetic antenna, bottom) error distribution.

The charge estimation, as per the time domain methods described above, yielded a varying error depending on two main factors: the distance to the PD source and the determination of the integration limits from the signals. For MA1 and MA2, most of the charge values fall into the 0-20 % error bins (774/1085 signals for MA1 and 697/1085 for MA2), proving that after 3 m (MA1) and 14.2 m (MA2), the attenuation and distortion of the PD signals are moderate. This resulted in very similar scatter plots for MA1 and MA2. The halving of the peak amplitude caused the larger scatter seen for MA3 after the PD pulse split into halves at the T-connector after

compartment 2 (see Figure 14). The peak reduction is also a reduction of the SNR of the signal, which strongly affects the correct determination of the integration limits.

This situation is illustrated in Figure 24 top, where the output of MA1 and MA3 are shown corresponding to a PD signal of 15 pC at the test cell. For the antenna MA1, the limits of the main peak of the cumulative integral were determined correctly by the algorithm, thus leading to a charge estimation of 13.8 pC. However, the limits were miscalculated for MA3, resulting in an overestimation of the charge of 24 pC.

On the other hand, improvements of the algorithms to determine the integration limits will result in the reduction of the scatter of the charge estimation. For example, when the integration limit is corrected to that corresponding to the red dotted line in the MA3 plot, the charge is better estimated to a value of 16 pC.

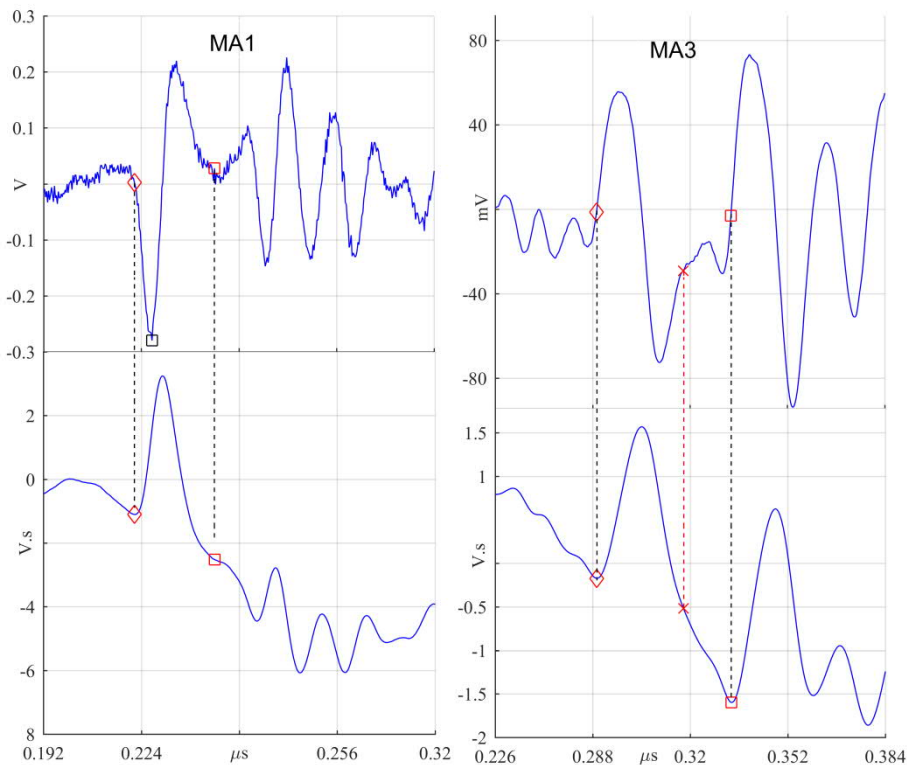


Figure 24. Integration limits for MA1 and MA3 for a reference charge of 15 pC. Top) antenna's output, bottom) cumulative integral of antenna's output.

4 LOCALIZATION

This section gives some insights into the localization capabilities of the measuring system based on magnetic antennas. The localization capabilities are studied using the data collected during the test 2.

In test 2, the PD source was located at the compartment 2, which means that the PD source was at 2.4 m from the MA2, at 4.25 m from MA3, and at approx. 14 m from the MA1. Considering that the PD pulse travels along the GIS as in a transmission line, it is expected that MA2 first detects the PD signal, then MA3, and finally, the MA1.

Figure 25 corroborates this expectation, showing that the PD pulse is measured first by MA2, 5.7 ns later is detected by MA3, and 46.7 ns later is measured by MA1; the peak value was used to determine the time of arrival.

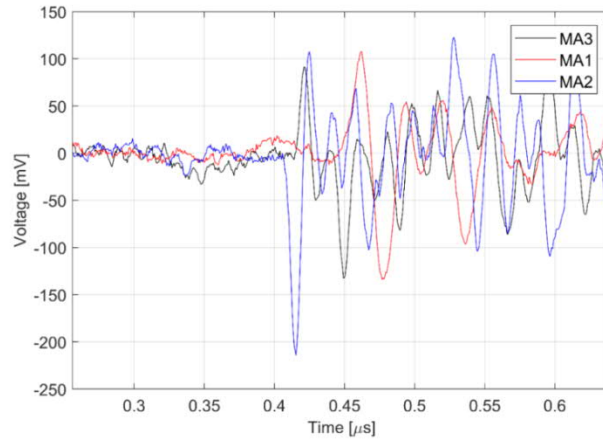


Figure 25. PD pulse measured at MA1, MA2, and MA3, in which only one loop is depicted.

Assuming that the speed of propagation is equal to the speed of light in vacuum, it is possible to estimate the distance between the defect and the magnetic antenna MA3 using equation (1).

$$x_{defect} = \frac{x_T}{2} - \frac{c * \Delta t}{2} \quad (1)$$

Where Δt is the time difference between MA2 and MA3, c is the speed of light in vacuum, x_T is the distance between the two antennas, and x is the distance between MA3 and the defect. Therefore, the estimated distance is:

$$x_{defect} = \frac{6.65 [m]}{2} - \frac{c * (-5.7 [ns])}{2} = 4.18 [m] \quad (2)$$

It means that the distance between the PD source and the magnetic antenna MA3 is 4.18 m, which is relatively closer to the real value mentioned before (4.25 m). Now, using the MA1, MA2, and the MA3, the estimated distance between the MA1 and the PD source is:

$$x_{defect} = \frac{11.2 [m]}{2} - \frac{c * (-46.7 [ns])}{2} = 12.60 [m] \quad (3)$$

PROJECT REPORT

In this case, the estimated distance between the MA1 and the defect is 12.60 m, having an absolute error of 1.11 m.



5 POST-PROCESSING TECHNIQUE FOR NOISE DISCRIMINATION.

Noise rejection problem.

Although the PD measurement has been exhaustively researched over the years, the separation of PD pulses from noise is one of the main challenges, especially in online applications for GIS systems. Noise contamination is one of the significant problems of PD detection because the noise, disturbances, and interferences can cause false indications of PD activity.

In GIS systems, the most extended PD detection technique is based on UHF couplers because it is less influenced by the noise, which is mainly concentrated at the low frequencies. The GIS enclosure shields the UHF sensors from external electromagnetic noise, allowing a low background noise, and resulting in high sensitivity. However, at the frequency range, in which the magnetic antenna operates, there is a significant presence of external noise having time-frequency characteristics similar to the partial discharge. These external disturbances affect the measuring system based on magnetic antennas presented before, causing a false indication of PD activity.

Several studies [10]–[19] have been conducted on the separation and denoising of PD pulses from noisy environments, being the wavelet transform the most extended technique because of its high capabilities on analyzing aperiodic signals with irregular and transition features, such as the PD pulses[19]. Among the wavelet techniques, the Discrete Wavelet Transform (DWT) is broadly used for denoising PD signals; the PD signals are decomposed in several wavelet coefficients, and then each coefficient is passed through a threshold (soft or hard) and followed by the reconstruction of the signal by taking the inverse wavelet transform.

However, the presence of external interferences having time-frequency characteristics similar to the partial discharge signals (pulse shaped disturbances) still one of the major problems of the existing denoising techniques. For instance, periodic pulse shaped interferences from power electronics or another periodic switching[11], PD and corona discharges from the external power system, electrical pulses from switching operations, lightings, etc.

To address the noise contamination, a technique for the separation of partial discharge signals from external disturbances has been developed for the PD measuring system based on magnetic antennas. The technique is based on the cross wavelet transform (XWT) analysis and in the support vector machine (SVM) classification algorithm. The main goal of the technique is the automatic recognition of PD signals and common-mode external disturbances being measured by the magnetic antennas. For the development of the technique, PD measurements were performed in the HV GIS, in which PD signals and external disturbances were measured. The wavelet analysis, the experimental test, the features extraction and analysis, the classification algorithm, and the separation results are described.

Experimental results and substantial information contained in the following sections were extracted from the journal paper “Partial Discharges and Noise Discrimination Using Magnetic Antennas, the Cross Wavelet Transform and Support Vector Machines” published in *Sensors*, 2020.



5.1 NOISE REJECTION TECHNIQUES

Several studies have been conducted on the separation and denoising of PD pulses from noisy environments, being the wavelet transform the most extended technique because of its high capabilities on analyzing aperiodic signals with irregular and transition features, such as the PD pulses. Among the wavelet techniques, the Discrete Wavelet Transform (DWT) is broadly used for denoising PD signals; the PD signals are decomposed in several wavelet coefficients, and then each coefficient is passed through a threshold (soft or hard) and followed by the reconstruction of the signal by taking the inverse wavelet transform.

However, the presence of external interferences having time-frequency characteristics similar to the partial discharge signals (pulse shaped disturbances) still one of the major problems of the existing denoising techniques; for instance, periodic pulse shaped interferences from power electronics or another switching, PD, and corona discharges from the external power system, electrical pulses from switching operations, lightings, etc. This external noise can lead to false indications of PD activity, corrupting the PD measurements.

In GIS systems, multiple UHF antennas are placed and recorded simultaneously, increasing the spatial sensitivity of the PD measurements and reducing the false indications. Deploying a set of PD sensors means that multiple waveforms are simultaneously acquired, providing extra useful information about the real nature of the phenomenon measured. Commonly, the PD measurement systems in GIS have an external signal named external trigger, which detects all the external disturbances coming from outside the GIS. The set of signals requires the identification of the relationships among them; for that purpose, tools like the correlation and trend analysis provide the significance of relationships among the signals recorded [20]. For instance, a pulse-shaped signal recorded only in one single UHF antenna may account as a PD signal, causing a low correlation among the signals and showing that the measurements are hardly related.

On the other hand, a signal acquired by all the antennas and the external trigger would have a high correlation and may indicate an external disturbance. However, if the signals are phase-shifted, these tools may not detect the correlation. For instance, the magnetic antenna loops have a phase shift of 180° between the signals, and thus the signals may appear uncorrelated. The cross-correlation and the cross-spectral analysis can detect the phase shift between both loops, but only as average values and in stationary signals. For analyzing the aperiodic PD signals measured, the most suitable tool is the Cross Wavelet Transform (XWT) because it shows the regions with high common power and reveals the local relative phase between the signals[20]. The Cross Wavelet Transform is part of the wavelet analysis[17], and it is a measure of similarity between two waveforms[21]. The XWT finds links between signals, because it gives a measure of the correlation between two time series in the time-frequency domain[17]. Therefore, it may be possible to apply the XWT in the separation of PD signals from noise and external disturbances in the magnetic antenna.

In [17], [22]–[24] the use of XWT has been reported in PD measurements, where in [17], the cross wavelet analysis was used in PD measurements to analyze the common power spectrum between two PD sensors located in the test object. In [23], [24], the XWT was applied in PD measurements in power transformers where the cross wavelet was applied to identify regions having high common power between the PD signals measured at different locations in the transformer. In [22], the XWT was used to discriminate and locate PD sources using acoustic measurements. Nevertheless, the application of XWT techniques for the removal of pulse-shaped external interferences in GIS systems has not been examined so far.

5.2 PD PULSES AND NOISE SIGNALS.

In section 2.1 was presented that the PD pulses travel inside the GIS compartment in the TEM mode of propagation due to the coaxial waveguide formed by the enclosure and the main conductor. Later, it was shown the magnetic antenna signals present a mirror-like symmetry for the PD pulses



traveling in the TEM mode, where the mirror-like symmetry is caused by the fact that the PD current flows homogeneously distributed in the enclosure, as in presented in Figure 26a.

On the other hand, for a common-mode noise signal, the current flow outside the enclosure (outside the coaxial waveguide). For instance, in Figure 26b, a common-mode signal cross-section representation is shown, where the propagation takes place in a parallel circle-plane waveguide. In this waveguide, the common-mode current does not flow homogeneously distributed in the surface of the enclosure and, its corresponding electromagnetic wave does not necessarily travel in the TEM mode. The common-mode signals are picked up by the magnetic antennas, but due to the difference in the propagation with respect to the PD pulses, the output signals are asymmetric.

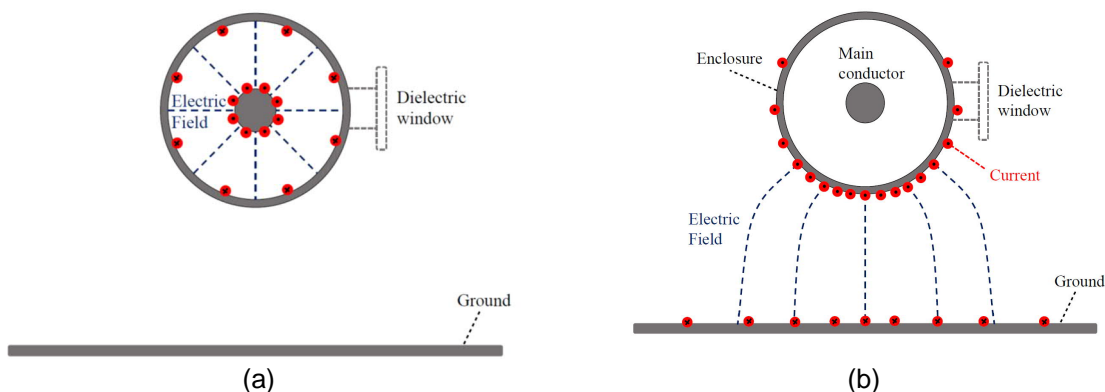


Figure 26. PD pulse cross-section propagation: (a) PD pulse. (b) Common-mode pulse [25].

Therefore, the evaluation of the magnetic antenna signals symmetry plays a crucial role in the separation of PD pulses from common-noise external disturbances. In this work, the cross wavelet transform (XWT) is deployed for the evaluation of the symmetry, resulting in a group of features that contains sufficient information to discriminate the PDs from the common-mode noise. The features are used for training a support vector machine (SVM) classifier, which can predict the nature (class) of a new input signal.

5.3 THE CROSS WAVELET TRANSFORM.

The symmetry evaluation of the signals requires the identification of the relationships between the signal output at the top-loop and the signal at the bottom-loop, for that purpose, tools like the correlation and trend analysis provide the significance of relationships between the signals recorded [13]. However, if the signals are phase-shifted, these tools may not detect the correlation. For instance, the magnetic antenna loops have a phase shift of 180° between the signals, and thus the signals may appear uncorrelated. The cross-correlation and the cross-spectral analysis can detect the phase shift between both loops, but only as average values and in stationary signals. For analyzing the pulse-shaped PD signals, the Cross Wavelet Transform (XWT) shows the regions with high common power and reveals the local relative phase between the signals [13]. The Cross Wavelet Transform is part of the wavelet analysis [9], and it is a measure of similarity between two waveforms [14]. The XWT finds links between signals, because it gives a measure of the correlation between two time series in the time-frequency domain [9]. In [9], [15]–[17] the use of XWT has been reported in PD measurements, where in [9] the cross wavelet analysis was used in PD measurements to analyze the common power spectrum between two PD sensors located in the test object. In [16], [17], the XWT was applied in PD measurements in power transformers where the cross wavelet was applied to identify regions having high common power between the PD signals measured at different locations in the transformer. In [15], the XWT was used to discriminate and locate PD sources using acoustic measurements. Nevertheless, the application of XWT techniques

for the removal of pulse-shaped external interferences in GIS systems has not been examined so far.

A wavelet is a small wave of limited duration that has zero mean. Wavelets are irregular, of limited duration, and non-symmetrical. Therefore, they are the best option for analyzing signals with anomalies, non-periodic signals, pulses, and –in general– events that start and stop within the signal [18].

The continuous wavelet transform (CWT) of a signal $x_n (n=1, \dots, N)$ is defined as follows:

$$W_n^x(s) = \sqrt{\frac{\delta t}{s}} \sum_{n'=1}^N x_{n'} \psi_0[(n' - n) \frac{\delta t}{s}] \quad (4)$$

Where s is the scale, δt is the time step, and ψ_0 is the mother wavelet. The asterisk $*$ denotes complex conjugation. The wavelet transform result is a matrix of wavelet coefficients $W_n^x(s)$. These wavelet coefficients have the information about the signal at the scale s and time position, which means that the CWT can be viewed as a mathematical tool that transforms a time domain signal x_n into a time-scale domain[20].

For analyzing non-periodic signals, the CWT is an appropriate tool because it obtains the time-frequency representation of the signal. However, the Cross Wavelet Transform (XWT) is a powerful tool for measuring the correlation between two signals in the time-frequency domain. The XWT is more appropriate at finding links between two signals than the CWT. The XWT is a measure of similarity between two waveforms [21], exposing regions with high common power and reveals information about the phase relationship. The XWT of two signals x_n and y_n is defined as:

$$W_n^{xy}(s) = W_n^x(s) W_n^{y*}(s) \quad (5)$$

Where the $W_n^x(s)$ and $W_n^y(s)$ are the CWT of x_n and y_n , respectively, and $*$ indicates the complex conjugate. The XWT is a complex number and can be decomposed into amplitude and phase using equation (6).

$$W_n^{xy}(s) = |W_n^{xy}(s)| e^{j \cdot \arg(W_n^{xy}(s))} \quad (6)$$

Where $|W_n^{xy}(s)|$ represents the XWT modulus (magnitude) and $\arg(W_n^{xy}(s))$ denotes the XWT argument (phase). The modulus of the XWT represents the cross-amplitudes of x_n and y_n [20], whereas the XWT argument provides an estimation of the local phase difference $\Delta\varphi_n^{xy}(s)$ between the two signals for each point in the time-frequency space[26]. In other words, $\Delta\varphi_n^{xy}(s)$ is the local relative phase between both signals[27]. To measure how coherent the XWT is in the time-frequency space, the XWT analysis uses the wavelet coherence, which is a mathematical tool defined as follows:

$$R_n^2(s) = \frac{|S(W_n^{xy}(s))|^2}{S(|W_n^x(s)|^2)S(|W_n^y(s)|^2)} \quad (7)$$

Where S is a smoothing operator in time and scale.

5.4 EXPERIMENTAL SETUP.

For building up the classification technique, PD measurements were conducted in the HV GIS present at the Delft University of Technology and described in section 2.3. The experiment used a HVDC source, three magnetic antennas, a corona PD defect, a horizontal electric dipole, and a digital oscilloscope. Figure 27 shows the GIS map for this test, where the location of the magnetic antennas, the electric dipole, and the PD defect are presented. The corona PD defect consisted of a needle connected to the main conductor at the compartment 1. With the HVDC source, -15 kV were applied to the GIS, causing PD discharges at the corona defect. A 1 m length horizontal electric dipole radiator was deployed to induce common-mode signals in the GIS. The horizontal dipole was placed in the middle of the GIS. It was connected to a fast pulse generator, creating common-mode external disturbances which were acquired by the PD measuring system. The signals picked up by the magnetic antennas were transmitted by identical coaxial cables to the digital oscilloscope, which sampled them simultaneously. The sampling frequency of the oscilloscope was set at 1.25 GS/s, recording 2.05 μ s per signal (each signal has N = 2564 samples).

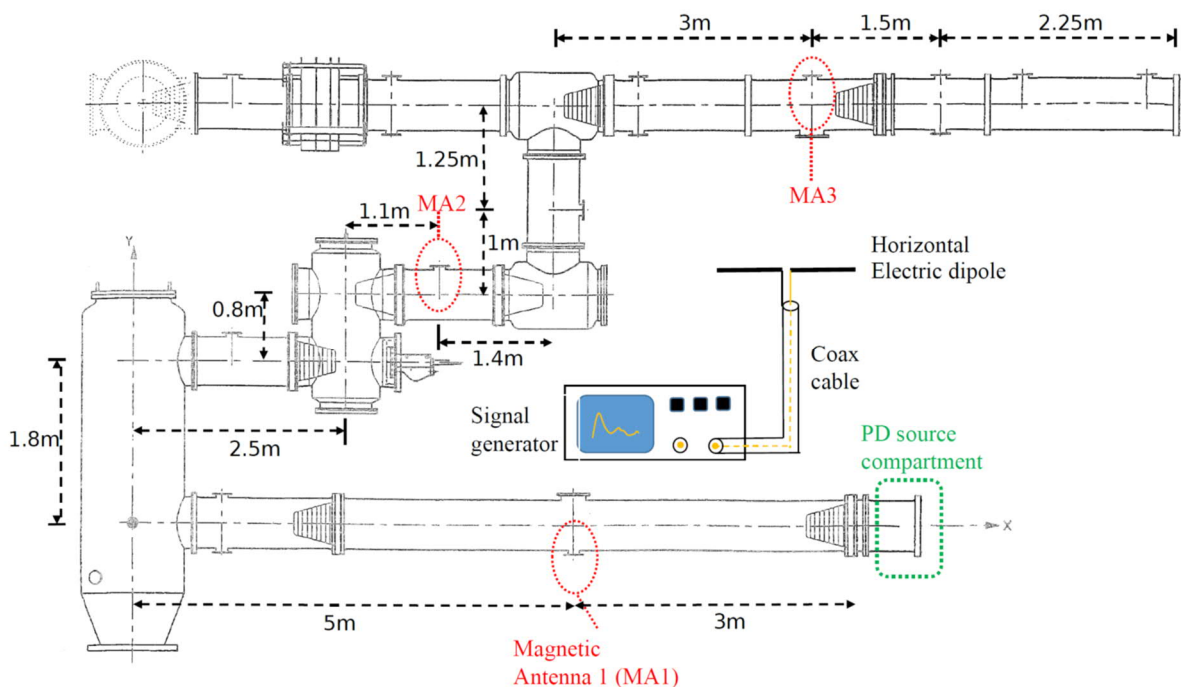


Figure 27. Test setup for noise separation [25].

Three experiments were realized, one with only the PD pulses, another one with only common-mode signals, and the last one with a combination of PD pulses and common-mode signals. In Table 3, a description of the experiments is given.

Table 3. Experiments overview.

Name	Type of signals	Pulses recorded per magnetic antenna
Test 1	Partial discharges	100
Test 2	External disturbances (common-mode signals)	100
Test 3	PDs and external disturbances.	1000 (81% are PDs)

In test 1, the HVDC was set at -15 kV, and the electric dipole radiator source was off. In test 2, the HVDC was switched off, and the electric dipole radiator source was on. In test 3, both the HVDC source and the electric dipole were on.

Figure 28a shows a PD pulse recorded by the MA1, whereas Figure 28b depicts a common-mode signal captured by the same antenna. As expected, in the PD signals, the first peak appears around the same time, have opposite polarities, similar magnitudes, and the characteristic mirror-like symmetry. On the contrary, the common-mode external disturbances do not present such asymmetry.

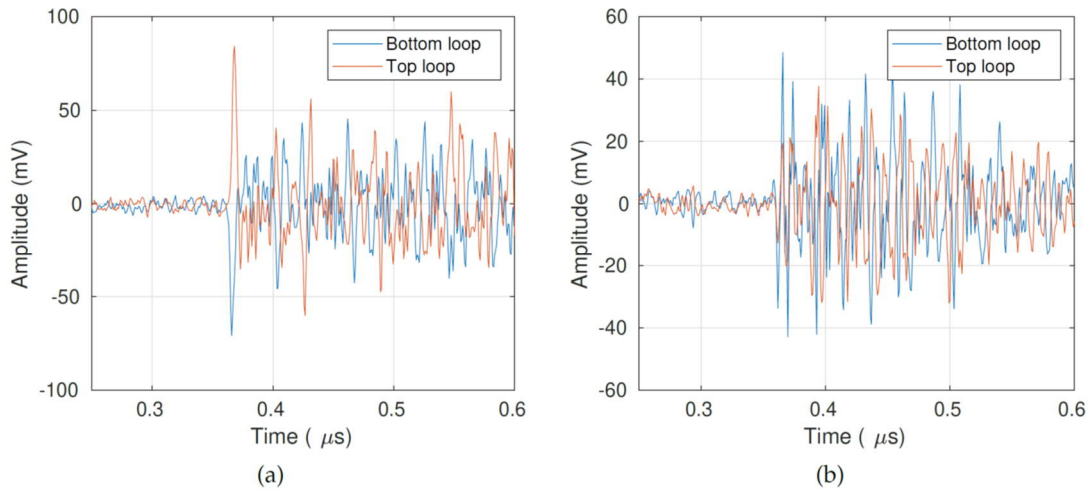


Figure 28. Signals captured by the MA1: (a) PD pulse. (b) Common-mode external disturbance [25].

For the evaluation of the symmetry in the signals presented in Figure 28, the wavelet coherence was computed for both signals, as is shown in Figure 29. The coherence was computed using the complex wavelet Morlet as mother. The signals were decomposed in 89 wavelet scales, equivalent to the frequency range from 1 MHz to 625 MHz. The wavelet coherence shows that the PD pulse and the external disturbance have a high correlation along the pulses. However, it does not indicate the polarity opposition present in the PD pulses. To consider the opposite polarity in the PD pulses, the local relative phase $\Delta\varphi_n^{xy}(s)$ is computed. Then, the elements in $\Delta\varphi_n^{xy}(s)$ having a local relative phase higher than 160° are selected, whereas the elements in $\Delta\varphi_n^{xy}(s)$ with a local relative phase lower than 160° are disregarded, as is shown in the equation (8). Opposite polarity means a local relative phase of 180° , but due to the signals discretization, the manufacturing differences, and the misalignments in the antenna installation, a lower local relative phase is expected.

$$ind\Delta\varphi_n^{xy}(s) = \begin{cases} 1, & \text{if } \Delta\varphi_n^{xy}(s) \geq 160^\circ \\ 0, & \text{if } \Delta\varphi_n^{xy}(s) < 160^\circ \end{cases} \quad (8)$$

The $ind\Delta\varphi_n^{xy}(s)$ is multiplied by the wavelet coherence, resulting in $R160_n^2(s)$ which is the wavelet coherence for the elements having a local relative phase higher than 160° .

$$R160_n^2(s) = R_n^2(s) \cdot ind\Delta\varphi_n^{xy}(s) \quad (9)$$

In Figure 30, the $R_{160}^2(s)$ is plotted for both the PD pulse and the common-mode external disturbance. This plot highlights the different polarities in the PD pulse because it shows a high and constant correlation between the signals along the PD duration. At the same time, the external disturbances do not present a clear and constant correlation along the signal duration.

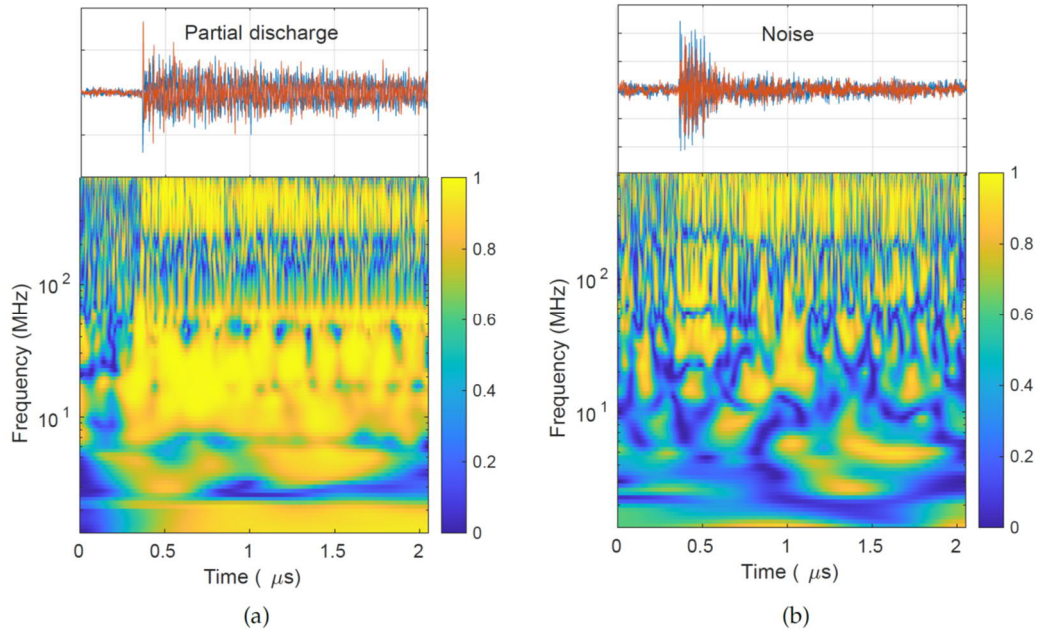


Figure 29. Wavelet coherence: (a) PD pulse. (b) Common-mode external disturbance [25].

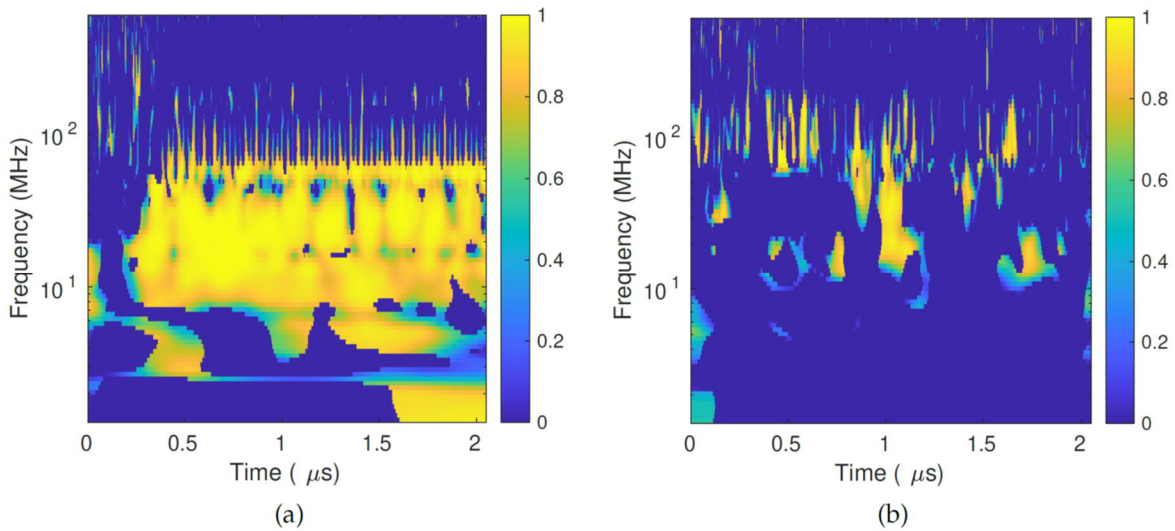


Figure 30. Wavelet coherence for a local relative phase higher than 160°: (a) PD pulse. (b) Common-mode external disturbance [25].

5.5 FEATURES EXTRACTION.

The $R_{160}^2(s)$ clearly indicates that it is an appropriate tool to evaluate the mirror-like symmetry of the PD pulses. However, the calculation of $R_{160}^2(s)$ for each signal results in a matrix, whose size, for this study, is 89x2564. This shows that there is some room for a reduction of the data dimensionality by computing the mean value of each scale in the wavelet coherence. Equation (10)

defines the mean of each scale in the wavelet coherence. By computing equation (10), the data dimensionality is reduced from an 89x2564 matrix to an 89 elements vector (89 features).

$$\hat{R}(s) = \frac{1}{N} \sum_{n=1}^N R160_n^2(s) \quad (10)$$

The wavelet coherence and its mean value are computed for the experiments listed in Table 3, resulting in the data sets presented in Table 4.

Table 4. Data sets computed.

Name	Type of signals	Data sets built by applying $\hat{R}(s)$	Data set size.
Test 1	Partial discharges	Data set 1	300 signals x 89 features
Test 2	External disturbances	Data set 2	300 signals x 89 features
Test 3	PDs and external disturbances.	Data set 3	3000 signals x 89 features

The reduction in the dimensionality gives way to the Principal Components Analysis (PCA) that helps to understand the data sets (learning from the data) [25]. The PCA is a tool for displaying and exploring multidimensional data by reducing the data complexity. In this study, each signal is represented by a vector with 89 features, making hard the visual analysis of the data; it is not possible to display 89 dimensions. The PCA is applied to the Data set 1 and 2, resulting in a 3D representation of the data, which is depicted in Figure 31. The first three components given by the PCA show the formation of four clusters, where one cluster represents the PD pulses in the MA1, the second one groups the PDs in the MA2, the third one the PD pulses in the MA3, and the fourth cluster groups the external disturbances captured by all the magnetic antennas.

The PCA indicates that the data the wavelet coherence together with the angle selection and the mean value $\hat{R}(s)$ are suitable tools for extracting relevant features for the separation of external disturbances and partial discharges. Therefore, it makes possible the automatic separation of PDs and common-mode external disturbances by fitting a supervised classifier such as the SVM.

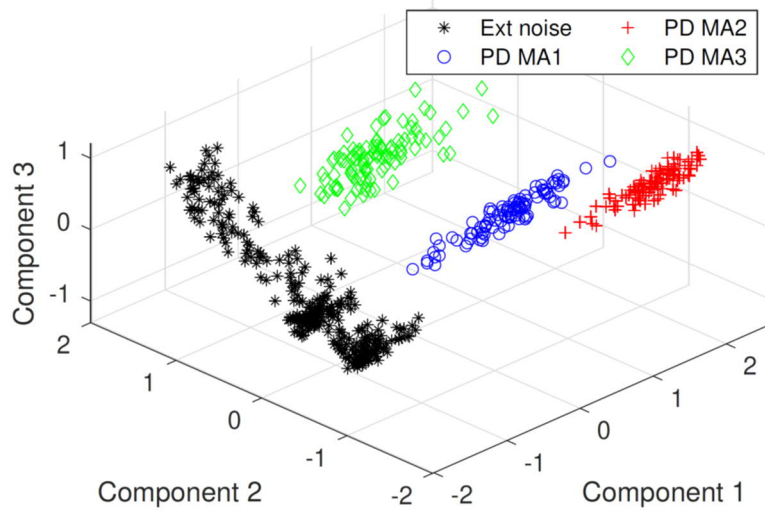


Figure 31. The first three components of the PCA applied to the Data set 1 and 2 [25].

5.6 SVM CLASSIFIER.

In this study, the separation of two types of signals (PDs and ext. dist.) is needed, meaning that a binary classification between the two classes is desired. In such a case, the SVM classifier is a tool for finding a separating hyperplane between the two classes. SVM have low generalization error avoiding over-fitting, is computationally inexpensive, and its results are easily interpreted. However, they work correctly only if the data is linearly separable. By plotting the first two components of the PCA in Figure 31, it is possible to conclude that the data is linearly separable because it forms two groups (one for each class) that can be separated by a line called hyperplane, as is shown in Figure 32. The separating hyperplane was arbitrarily placed in the middle of the two groups, and it works as a decision boundary because all the points at the left of the hyperplane can be classified as *external disturbances* and all the points at the right can be label as *partial discharges*.

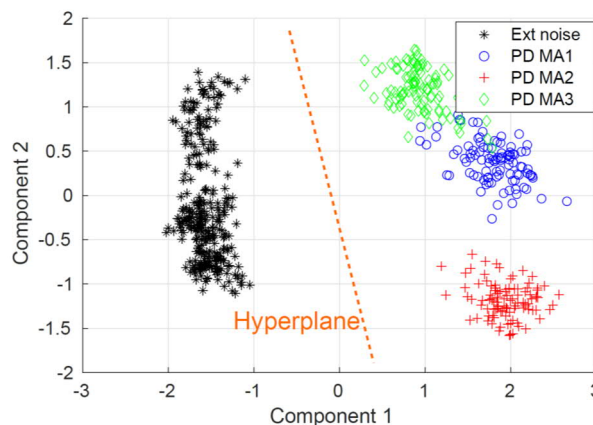


Figure 32. The first two components of the PCA applied to the Data set 1 and 2 [25].

A SVM algorithm was trained using the Data set 1 and 2, which were taken as *training set*. The signals in the data set 1 were labelled as *partial discharges*, while the signals in the data set 2 as *external disturbances*. The performance of the SVM classifier was evaluated using the data set 3 as *validation set*. The class (PD or ext. dist.) of each signal in the data set 3 was manually verified. The

data set 3 has 3000 pulses, in which 2427 are partial discharges, and 573 are common-mode external disturbances.

The performance of the SVM classifier is tested with the validation set, getting an error rate of 0.33 %. The confusion matrix is depicted in Figure 33; 2427 PDs were correctly classified as PD, 563 external disturbances were successfully labelled, and 10 external disturbances were misclassified as PD. These results show that the XWT based analysis, together with the SVM classifier, are useful tools to identify PD pulses from common-mode external disturbances. Therefore, this denoising technique provides a tool for addressing noise contamination in the PD measuring system based on magnetic antennas.

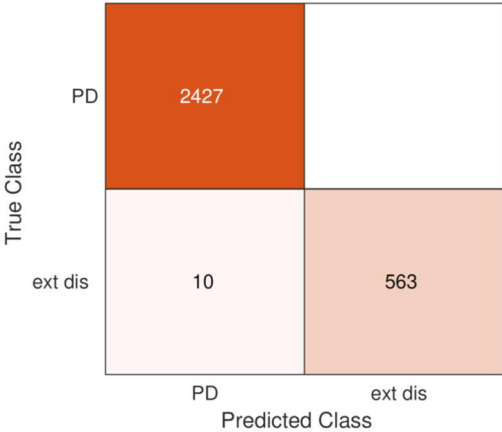


Figure 33. Confusion matrix validation set [25].

6 TESTING OF THE PD MONITORING SYSTEM IN AN ABB 320 KV HVDC GIS.

In the previous chapters, a new PD measuring system for GIS has been introduced, showing that it is a feasible option for GIS systems because of its high sensitivity, charge estimation, and defect localization capabilities, and its processing techniques for noise discrimination. However, this PD measuring system has only been tested in one HV GIS, and therefore, additional testing is required to validate the measuring system in different GIS systems. For that reason, the PD monitoring system based on magnetic antennas was deployed in the ABB HVDC GIS located at Kema Laboratories in Arnhem, The Netherlands. This HVDC GIS was subjected to long-term testing to confirm the reliability of the system under real service conditions. The long-term testing consisted of three phases, which are the pretest, the long-term voltage test, and the subsequent test. The HVDC GIS test pole, Figure 34, consists of a bus-duct ring that is connected to the high voltage DC through a SF₆ to air bushing. The GIS ring includes 8 gas compartments, 31 m busbar with straight, L, X, and T elements, 8 partition insulators, 14 support insulators, an RC divider, a zero-flux current sensor, switching devices, internal arc detection, and density monitoring, and a PD monitoring system based in UHF antennas.

The PD testing was performed using an HV DC source, an HV AC source, three magnetic antennas, an HFCT (Bergoz HFCT with 3.92 kHz–1.11 GHz bandwidth), and a digital oscilloscope. The magnetic antennas (MA1, MA2, and MA3) were installed in the GIS in the positions depicted in Figure 34. For the installation of the antennas, three UHF couplers were removed from the coupler windows. Figure 35a shows one of the coupler windows with its UHF coupler removed, and Figure 35b displays the MA2 installed in the coupler window of Figure 35a. Each magnetic antenna was connected to a decoupling capacitor (parallel of 2 x 0.056 μF) and a trans-impedance amplifier (Femto HCA-40M-100K-C).

The test cell in Figure 36a, with an inception voltage below 10 kV DC, was used for producing corona-type discharges. The test cell produces corona discharges ranging from 10 pC to 50 pC and is filled with SF₆ at 10000 Pa. The test cell was connected between the GIS main conductor and the external enclosure, as is depicted in Figure 36b and Figure 36c. For measuring the PD current at the source, an HFCT was installed through the rod that is connecting the enclosure and the test cell.

The signals picked up by the magnetic antennas, and the HFCT were transmitted by identical coaxial cables to a Tektronix MSO58 digital oscilloscope, which sampled them simultaneously in Fast Frame Acquisition. The sampling frequency of the oscilloscope was set at 1.25 GS/s, and the trigger was set in the HFCT located at the PD source.

Two tests were performed, one under HV AC and the second one under HV DC. In the first test, 5 kV_{rms} were applied to the GIS using the HV AC source. The first test aimed to identify the phase-resolved PD pattern of the corona test cell. In the second test, corona discharges were produced by applying -8 kV DC to the GIS using the HV DC source. The goal of the second test was to check the sensitivity, the charge estimation performance, and the localization capabilities of the PD measuring system installed in the ABB HVDC GIS.



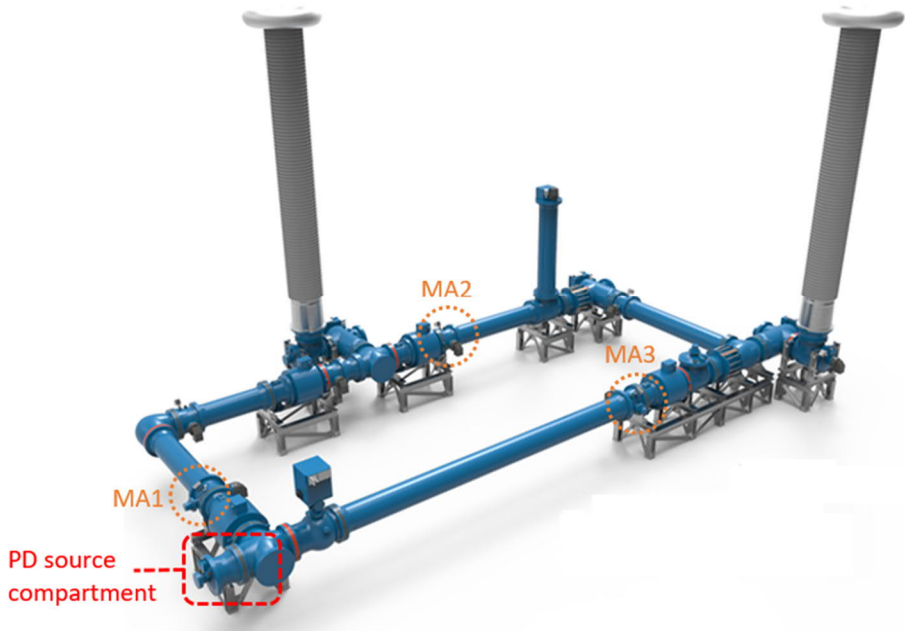


Figure 34. ABB HVDC GIS.



Figure 35. (a) Coupler window without the UHF antenna. (b) Coupler window with the magnetic antenna.

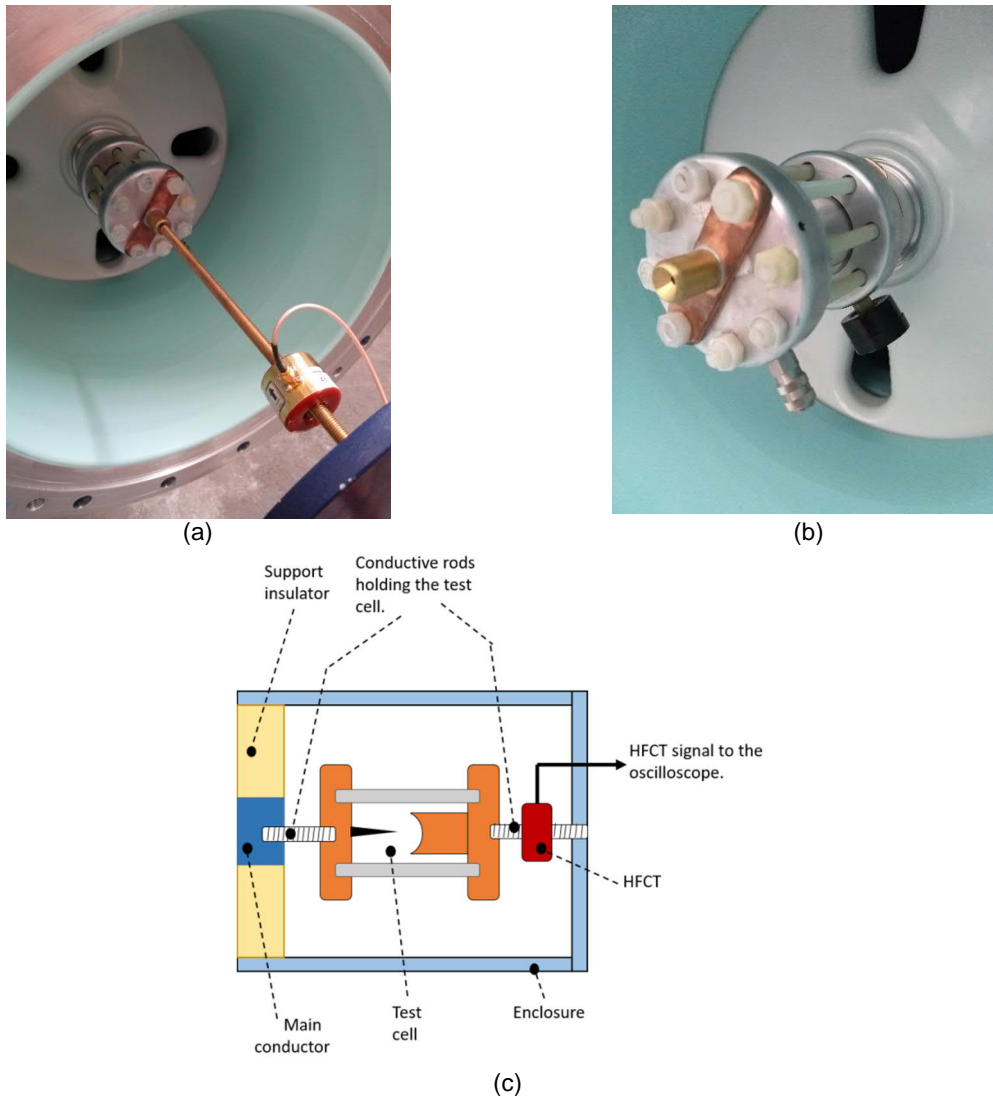


Figure 36. (a) Test cell connection to the GIS. (b) Test cell. (c) Test cell schematic.

6.1 RESULTS.

In the first test, PD pulses were produced by applying $-5 \text{ kV}_{\text{rms}}$ with the HV AC source. Figure 37 displays the Phase Resolved PD (PRPD) pattern for the PD measurements conducted in this test. The PRPD was realized by estimating the apparent charge of the signals measured by the HFCT located at the PD source. The shape of the PRPD indicates a clear corona-type discharge in which the needle is connected to the HV electrode (PD only in the negative cycle). These results show a corona-type discharge producing pulses with a charge ranging from 10 pC to 50 pC , which is convenient to study the PD monitoring system capabilities.

In the second test, negative HVDC (-8 kV) was applied to the test cell to produce PD. In this test, the PD measuring system simultaneously measured 1000 PD signals in all the PD sensors deployed in the GIS (the magnetic antennas and the HFCT), and therefore 7000 signals were recorded during the measurement; 1000 signals corresponding to the HFCT, and 2000 to each of the magnetic antennas. In Figure 38, a PD pulse captured by the HFCT and the magnetic antenna is depicted, showing that all the sensors were able to detect the PD signal. As expected, the magnetic antenna

signals show that the first peak of both loops appears around the same time, the signals have different polarities and a pseudo-mirror-like symmetry. The MA2 shows the smallest voltage magnitude because it is the farthest antenna to the PD source location (approx. 10 m away from the PD source compartment). These results conclude that the pulse propagation and the PD measuring system behave as they do in the TU Delft GIS, indicating the generalization of the concepts in which the measuring system was built.

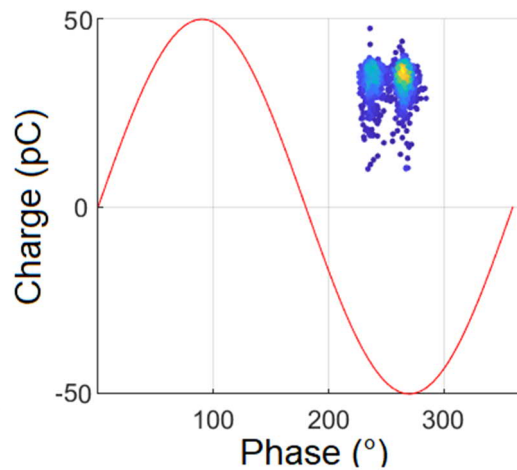
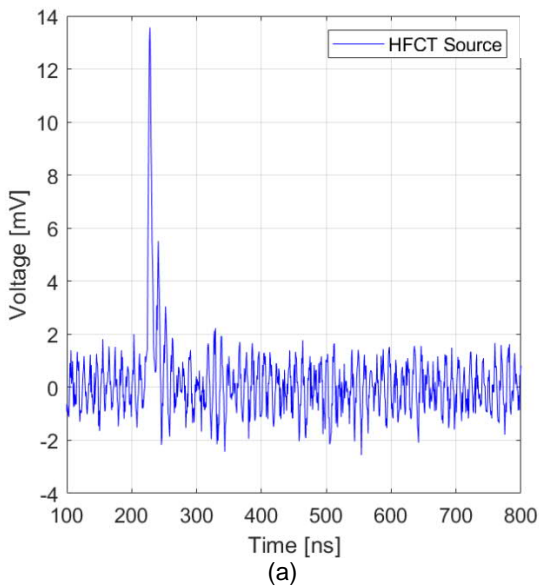
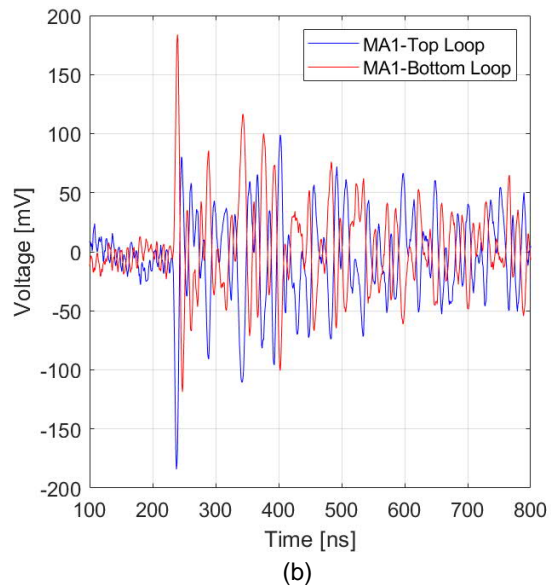


Figure 37. PRPD pattern.



a)



b)

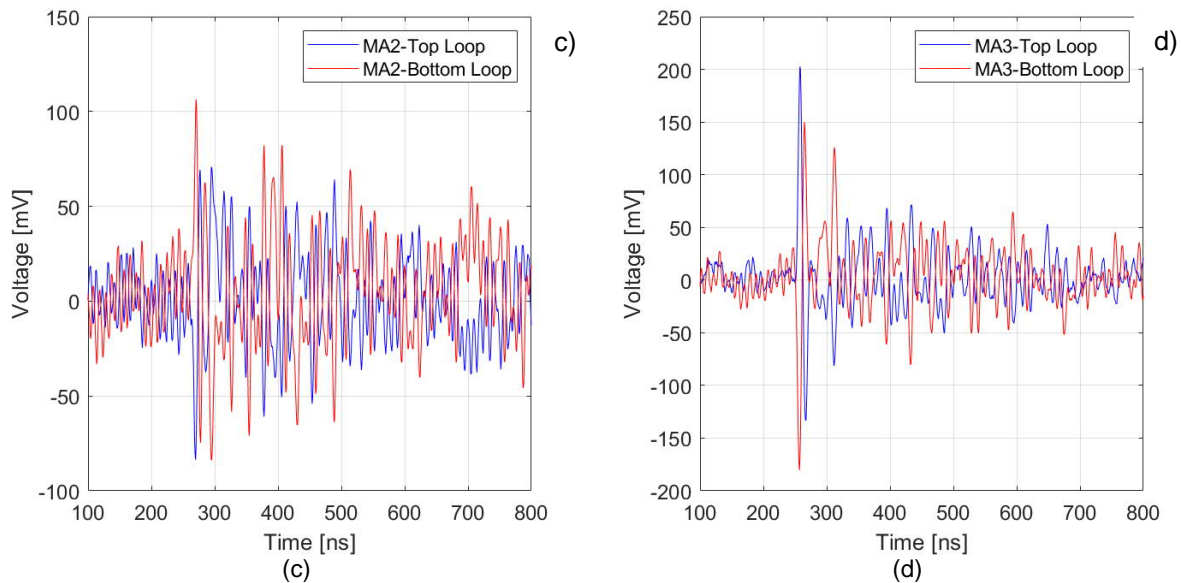


Figure 38. PD pulse measured by (a) the HFCT, (b) MA1, (c) MA2, (d) MA3.

6.2 SENSITIVITY.

The measuring system sensitivity was addressed by using the results obtained in the second test. The ability to detect PD pulses was checked by analyzing the response of the magnetic antennas to the minimum charge detected during the measurements; the minimum PD charge detected was 11.30 pC (measured by the HFCT). As in section 2.3.3, the detection level was addressed by applying these three criteria: the peak amplitudes of both loops are synchronized, the peak magnitude is at least two times the background noise, and the average power indicates a pulse.

Figure 39a shows the signal measured by the MA1 (the closest to the source) for the pulse having 11.30 pC apparent charge. In the signal displayed can be seen that both peaks occurred at the same time, the peak magnitudes are at least three times higher than the background noise, and the average power shows a significant rising of the power around the PD pulse. As the closest antenna, the farthest antenna (MA2) detects the PD pulse having 11.30 pC apparent charge, which is confirmed by the three criteria applied to the signal in Figure 39b; both peaks occurred at the same time, the peak magnitudes are at least two times higher than the background noise, and the average power shows a significant rising of the power around the PD pulse.

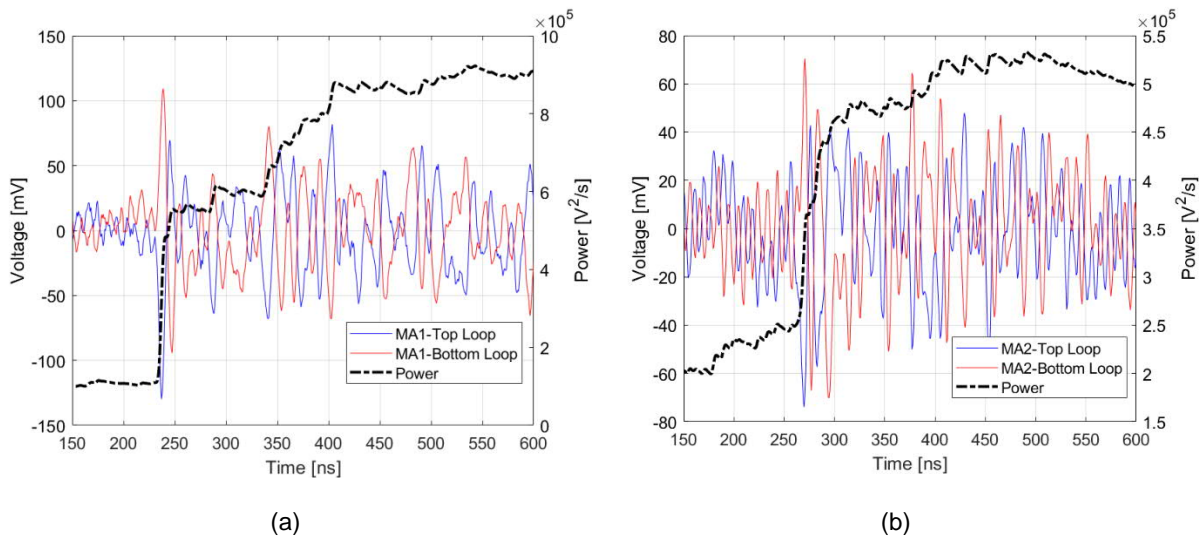


Figure 39. PD pulse having 11.30 pC apparent charge. (a) MA1. (b) MA2.

6.3 CHARGE ESTIMATION.

For the long-term testing, the ABB GIS was provided with a whole set of components, as listed in the introduction of this chapter. As long as the propagation of PD signals is concerned, all these components represent changes of impedance, and the loop arrangement of the GIS implies that the signals are halved before reaching any of the magnetic antennas. To check the all-together effects of distortion and attenuation of the PD signals on the charge estimation, the same procedure as with the GIS at TU Delft was also applied to this GIS.

Thus, the charge, as measured by HFCT next to the test cell, was used as the reference charge and compared to the charge as calculated by the integration method. Another similarity is that the analysis was limited reference signals with small values of charge. In this exercise, the smallest PD signals produced by the test cell resulted in charges in the range of 10-50 pC. PD signals with large peak amplitudes, although convenient for charge estimation, might hit the small-signal limit of the Femto HCA-40M-100K-C amplifiers. In such a case, the output signal will be distorted, rendering the charge analysis invalid. 1000 signals were synchronously acquired at a sampling rate of 1.25GS/s.

As opposed to the study case in TU Delft, where a calibration rig was available, in this study case calculating the calibration factor K_c became the objective of the tests. The former stands on the assumption that there exists a linear correlation between the charge produced by the test cell and the response from the antennas despite the differences in geometry and propagation characteristics of the GIS.

The results, displayed similarly as those in Figure 23, are reported in Figure 41. The compactness of the values around the reference black line accounts for the high degree of correlation of the data. Two essential remarks are worth mentioning at this point. First, $K_{cABBGIS}$ was assumed $2 \times (1.3 \times 7.1862^{\wedge}5)$, i.e., the same calibration factor applied to TU Delft GIS. Both GIS have similar diameters for the compartments and main conductor. Therefore, it is reasonable to expect a similar value of K_c . Second, the factor of 2 was necessary since the PD signals split before reaching any of the antennas. In TU Delft GIS, this was the case for antenna MA3 but not for antenna MA1 because antenna MA1 was located before the T-shaped compartment causing the split of the signal.

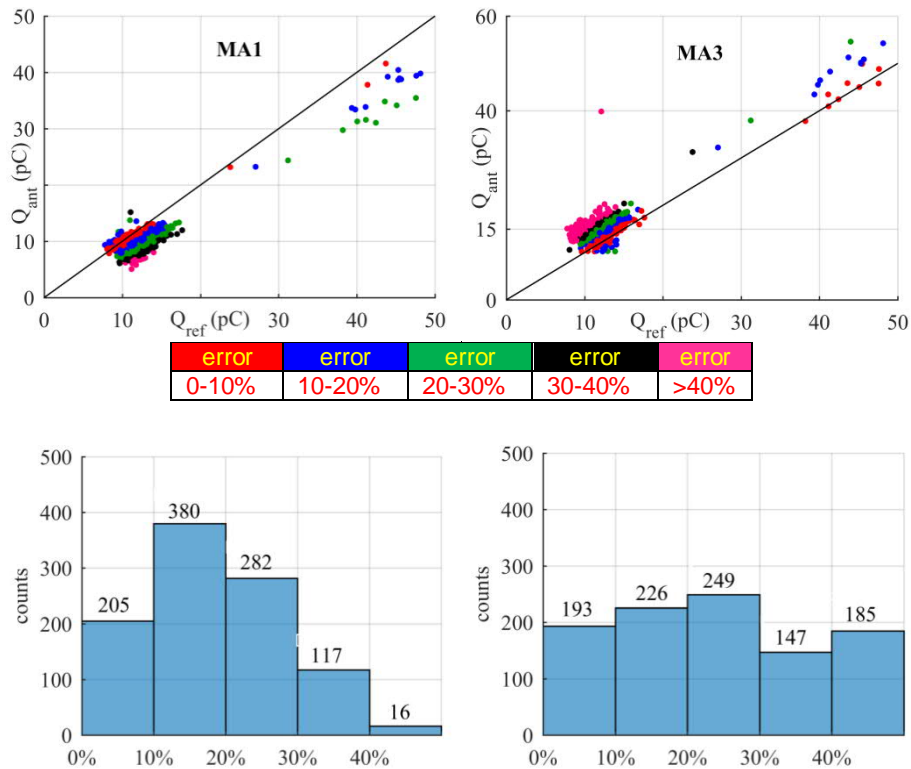


Figure 41. top) charge estimation and bottom) error distribution when $K_{C_{ABBGIS}}=2x(1.3x7.1862^5)$.

When looking at the plots in Figure 41, it is noticeable that the error tends to distribute around a central value as opposed to the skewed distribution of the results from TU Delft (Figure 23). The scatter is then higher. The reference line in the charge plots shows a complementary correlation: for MA1, the value of K_c seems to fall short but to be excessive for MA3.

A plausible hypothesis for this behaviour lies in the assumption that the PD pulses split into halves just at the injection point. Conversely, as shown in Figure 42, when $K_{C_{ABBGIS}}$ (MA1) and $K_{C_{ABBGIS}}$ (MA3) were increased and decreased by 20% respectively, the error distribution became left-skewed, meaning a significant reduction in the error in the charge estimation.

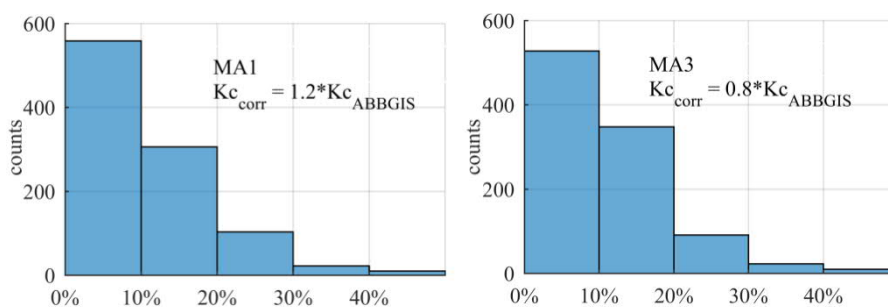


Figure 42. Error distribution when $K_{C_{ABBGIS}}$ has been corrected.

Worth noticing that this study is not considering the calculation of the propagation paths, the difference in characteristics impedances, nor the possible superposition error encountered by the narrow bandwidth of the antennas compared to the actual bandwidth of the PD pulse. The PD signals reach the antennas according to the transmission paths along which they are propagating. However, using different calibration factors seems to be a reasonable and practical method to

compensate for the differences in the complex propagation paths of the PD signals. This is supported by the reduction of the scatter in the charge estimation observed in the results.

6.4 LOCALIZATION.

The GIS map in Figure 43 gives detailed information on the GIS dimensions and the position of each magnetic antenna. The MA1 was placed at 1.83 m from the source, the MA2 at 10.1 m, whereas the MA3 at 6.925 m from the PD source.

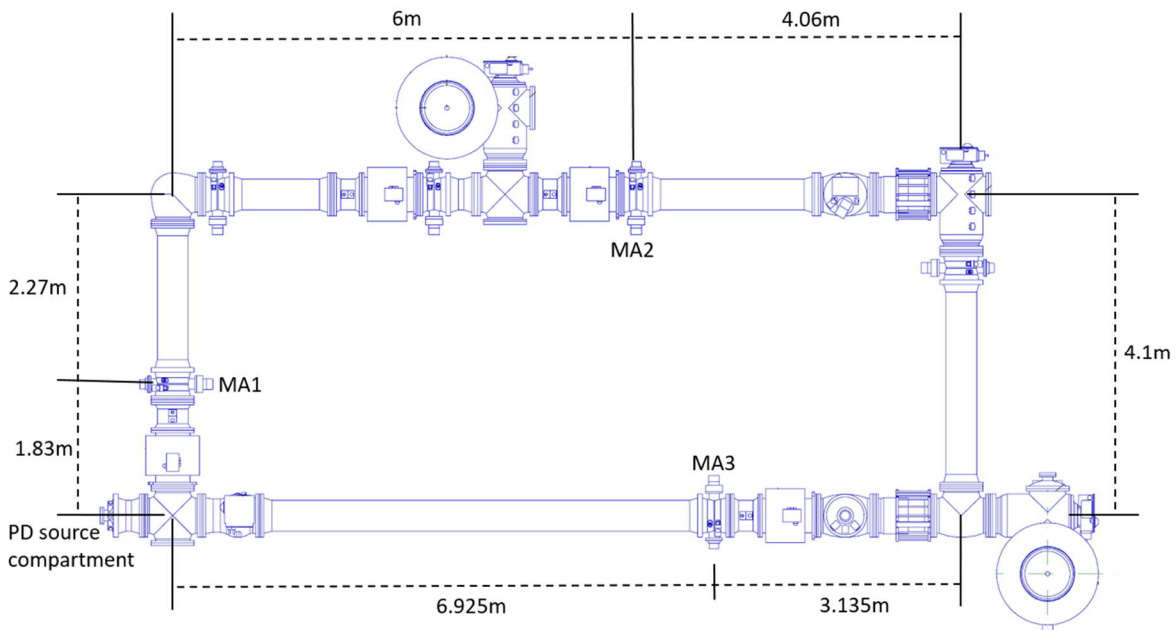


Figure 43. ABB GIS map.

In section 4 was shown that, by using the time of arrival of the PD pulses and equation (1), it is possible to estimate the localization of the PD source. In this study case, Figure 44 shows that a PD pulse is measured first by MA1, 18.4 ns later is captured by MA3, and 31.6 ns later is recorded by MA2. Again, the peak value determines the time of arrival.

The total distance between MA1 and MA3 is 8.755 m and having a speed of propagation equal to the speed of light in vacuum, the estimated distance between MA1 and the defect is equal to:

$$x_{defect} = \frac{8.755 \text{ m}}{2} - \frac{c * (18.4 \text{ ns})}{2} = 1.6175 \text{ [m]} \quad (12)$$

Therefore, the distance between the PD source and MA1 is 1.6175 m, which is slightly deviated from the real value of 1.83 m. Using the MA2 and the MA3, the estimated distance between the MA3 and the PD source is:

$$x_{defect} = \frac{17.05 \text{ m}}{2} - \frac{c * (31.6 - 18.4 \text{ ns})}{2} = 6.545 \text{ m} \quad (13)$$

In this case, the estimated distance between the MA3 and the defect is 6.545 m, having an absolute error of 0.38 m.

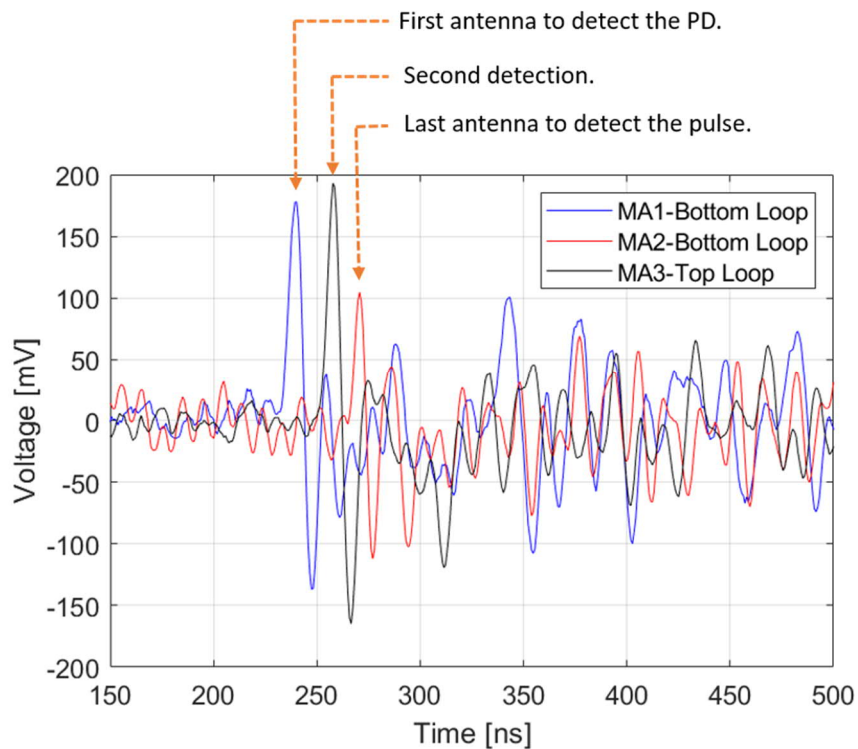


Figure 44. PD pulse measured at MA1, MA2, and MA3, in which only one loop is depicted.

7 CONCLUSION.

In this report, D15.5, a new magnetic sensor, and a detection system for partial discharge monitoring of HVDC GIS, has been researched. The measuring system is based on magnetic antennas that are placed in the existing coupler windows present in the GIS compartments. This new detection technique is capable of monitoring the PD activity with high sensitivity, estimate the PD apparent charge and locate the PD source using the time of arrival.

In the low frequency range, a PD pulse travels inside the GIS as in transmission line, generating an induced voltage in the coupler windows in which the UHF couplers are commonly installed. A magnetic sensor, consisting of two loops, was developed to capture the voltage induced by the PD current. The magnetic antenna was built using coaxial cables and is tuned at low frequency range of the PD signals.

The PD measurements performed in two real-size GIS showed that a magnetic antenna is a feasible option for PD monitoring in DC and AC GIS. The experimental results indicated that the magnetic antenna can detect small partial discharges in the range of pC. An important feature of the magnetic antennas is the possibility to estimate the PD apparent charge, where the results coming from the PD measurements in the two GIS showed a good correlation between the estimated charge values and the real charge injected by the PD at the source. Additionally, it has been proven the PD source localization capabilities of the measuring system based on magnetic antennas.

A useful tool for noise separation, in the PD measurements conducted with magnetic antennas, has been developed. The technique uses machine learning algorithms, and the wavelet transform for automatically discriminate noise from partial discharges.



8 BIBLIOGRAPHY

- [1] G. of the Netherlands, "Offshore wind energy," 2019. [Online]. Available: <https://www.government.nl/topics/renewable-energy/offshore-wind-energy>.
- [2] U. Schichler *et al.*, "UHF partial discharge detection system for GIS: Application guide for sensitivity verification: CIGRE WG D1.25," *IEEE Trans. Dielectr. Electr. Insul.*, vol. 23, no. 3, pp. 1313–1321, 2016.
- [3] M. Sawada *et al.*, "Influence of metal flange cover of insulation spacers on propagation properties of PD-induced electromagnetic wave in GIS," in *2008 International Conference on Condition Monitoring and Diagnosis*, 2008, pp. 437–442.
- [4] M. Hikita, S. Ohtsuka, S. Okabe, J. Wada, T. Hoshino, and S. Maruyama, "Influence of disconnecting part on propagation properties of PD-induced electromagnetic wave in model GIS," *IEEE Trans. Dielectr. Electr. Insul.*, vol. 17, no. 6, pp. 1731–1737, 2010.
- [5] M. Hikita *et al.*, "Propagation properties of PD-induced electromagnetic wave in GIS model tank with T branch structure," *IEEE Trans. Dielectr. Electr. Insul.*, vol. 18, no. 1, pp. 256–263, 2011.
- [6] M. Hikita, S. Ohtsuka, J. Wada, S. Okabe, T. Hoshino, and S. Maruyama, "Propagation properties of PD-induced electromagnetic wave in 66 kV GIS model tank with L branch structure," *IEEE Trans. Dielectr. Electr. Insul.*, vol. 18, no. 5, pp. 1678–1685, Oct. 2011.
- [7] A. Rodrigo-Mor, F. Muñoz, and L. Castro-Heredia, "A Novel Antenna for Partial Discharge Measurements in GIS Based on Magnetic Field Detection," *Sensors*, vol. 19, no. 4, p. 858, Feb. 2019.
- [8] A. Rodrigo Mor, L. C. Castro Heredia, and F. A. Muñoz, "A magnetic loop antenna for partial discharge measurements on GIS," *Int. J. Electr. Power Energy Syst.*, vol. 115, p. 105514, Feb. 2020.
- [9] F. Muñoz-Muñoz and A. Rodrigo-Mor, "Partial Discharges and Noise Discrimination Using Magnetic Antennas, the Cross Wavelet Transform and Support Vector Machines," *Sensors*, vol. 20, no. 11, p. 3180, Jun. 2020.
- [10] H. Zhang, T. R. R. Blackburn, B. t. T. Phung, and D. Sen, "A novel wavelet transform technique for online partial discharge measurements. 1. WT denoising algorithm," *IEEE Trans. Dielectr. Electr. Insul.*, vol. 14, no. 1, pp. 3–14, Feb. 2007.
- [11] L. Satish and B. Nazneen, "Wavelet-based denoising of partial discharge signals buried in excessive noise and interference," *IEEE Trans. Dielectr. Electr. Insul.*, vol. 10, no. 2, pp. 354–367, Apr. 2003.
- [12] M.-X. Zhu *et al.*, "Partial discharge signals separation using cumulative energy function and mathematical morphology gradient," *IEEE Trans. Dielectr. Electr. Insul.*, vol. 23, no. 1, pp. 482–493, Feb. 2016.
- [13] F. Alvarez, J. Ortego, F. Garnacho, and M. A. Sanchez-Uran, "A clustering technique for partial discharge and noise sources identification in power cables by means of waveform parameters," *IEEE Trans. Dielectr. Electr. Insul.*, vol. 23, no. 1, pp. 469–481, Feb. 2016.
- [14] R. Albarracin, G. Robles, J. M. Martinez-Tarifa, and J. Ardila-Rey, "Separation of sources in radiofrequency measurements of partial discharges using time–power ratio maps," *ISA Trans.*, vol. 58, pp. 389–397, Sep. 2015.
- [15] G. Robles, E. Parrado-Hernández, J. Ardila-Rey, and J. M. Martínez-Tarifa, "Multiple partial discharge source discrimination with multiclass support vector machines," *Expert Syst. Appl.*, vol. 55, pp. 417–428, Aug. 2016.
- [16] J. A. Ardila-Rey, J. M. Martinez-Tarifa, and G. Robles, "Automatic selection of frequency bands for the power ratios separation technique in partial discharge measurements: part II, PD source recognition and applications," *IEEE Trans. Dielectr. Electr. Insul.*, vol. 22, no. 4, pp. 2293–2301, Aug. 2015.
- [17] D. Dey, B. Chatterjee, S. Chakravorti, and S. Munshi, "Cross-wavelet transform as a new paradigm for feature extraction from noisy partial discharge pulses," *IEEE Trans. Dielectr.*

- Electr. Insul.*, vol. 17, no. 1, pp. 157–166, Feb. 2010.
- [18] I. Shim, J. J. J. Soraghan, and W. H. H. Siew, "Detection of PD utilizing digital signal processing methods Part 3: open-loop noise reduction," *IEEE Electr. Insul. Mag.*, vol. 17, no. 1, pp. 6–13, Jan. 2001.
- [19] X. Ma, C. Zhou, and I. J. Kemp, "Interpretation of wavelet analysis and its application in partial discharge detection," *IEEE Trans. Dielectr. Electr. Insul.*, vol. 9, no. 3, pp. 446–457, Jun. 2002.
- [20] A. Prokoph and H. El Bilali, "Cross-Wavelet Analysis: a Tool for Detection of Relationships between Paleoclimate Proxy Records," *Math. Geosci.*, vol. 40, no. 5, pp. 575–586, Jul. 2008.
- [21] S. Banerjee, S. Member, and M. Mitra, "Application of Cross Wavelet Transform for ECG Pattern Analysis and Classification," *IEEE Trans. Instrum. Meas.*, vol. 63, no. 2, pp. 326–333, 2014.
- [22] S. Biswas, D. Dey, B. Chatterjee, and S. Chakravorti, "Cross-spectrum analysis based methodology for discrimination and localization of partial discharge sources using acoustic sensors," *IEEE Trans. Dielectr. Electr. Insul.*, vol. 23, no. 6, pp. 3556–3565, Dec. 2016.
- [23] H. Suryavanshi, J. Velandy, and M. Sakthivel, "Wavelet power ratio signature spectrum analysis for prediction of winding insulation defects in transformer and shunt reactor," *IEEE Trans. Dielectr. Electr. Insul.*, vol. 24, no. 4, pp. 2649–2659, 2017.
- [24] D. Dey, B. Chatterjee, S. Chakravorti, and S. Munshi, "Rough-granular approach for impulse fault classification of transformers using cross-wavelet transform," *IEEE Trans. Dielectr. Electr. Insul.*, vol. 15, no. 5, pp. 1297–1304, Oct. 2008.
- [25] G. James, D. Witten, T. Hastie, and R. Tibshirani, *An Introduction to Statistical Learning*, vol. 103. New York, NY: Springer New York, 2013.
- [26] M. R. Jury, "Tropical monsoons around Africa: Stability of El Niño–Southern Oscillation associations and links with continental climate," *J. Geophys. Res.*, vol. 107, no. C10, 2002.
- [27] A. Grinsted, J. C. Moore, and S. Jevrejeva, "Application of the cross wavelet transform and wavelet coherence to geophysical time series," *Nonlinear Process. Geophys.*, vol. 11, no. 5/6, pp. 561–566, Nov. 2004.

